Molecular Orbital Study of Apatite ($Ca_5(PO_4)_3OH$) Nucleation at Silica Bioceramic Surfaces

Nita Sahai* and John A. Tossell

Department of Chemistry and Biochemistry, University of Maryland, College Park, Maryland 20742

Received: October 7, 1999; In Final Form: January 4, 2000

Silica bioceramics are used as prosthetic bone and dental implants because they promote apatite formation at their surfaces when immersed in simulated body fluids of composition similar to human blood plasma. Apatite formation occurs in stages, but the reaction pathway remains unresolved. We have used molecular orbital calculations to model the interactions of Ca^{2+}, $H_2PO_4^-$, HPO_4^{2-}, and H_2O with bioceramic surface sites represented by $Si_7O_{12}H_{10}$, $Si_4O_8H_8$, and $Si_3O_6H_6$ to determine the reaction sequence for apatite nucleation. Predicted reaction energies, vibrational frequencies, and ^{29}Si, ^{31}P, and ^{43}Ca NMR shifts were used as probes of the stable intermediates during reaction progress. Energies and vibrational frequencies were calculated using effective core potentials and valence double-ζ basis sets. Most NMR shifts were calculated using the 3-21G* basis, and using the 6-31G* basis for selected clusters. With increasing pH above the point of zero charge of silica, (pzc $\approx$ 3) the stability of the calcium surface complexes on the Si 3-ring ($[Si_3O_6H_6]$) is predicted to be outer-sphere < inner-sphere < surface-hydroxide. Comparison of calculated ^{29}Si and ^{31}P NMR shielding trends of Si 3- and 4-rings ($Si_3O_6H_6$ and $Si_4O_8H_8$, respectively) with experimental trends for bioceramic reacting with SBF suggest that (i) the partially deprotonated 3-ring is the active surface site, because it promotes calcium ion dehydration as calcium adsorbs, (ii) formation of [SiO−Ca−OPO_3H] bonds is energetically preferred over direct Si−O−P bonds, and (iii) an acidic precursor with bidentate Ca>OPO_3H bonds nucleates rapidly (minutes to 1 h) at the bioceramic surface. The precursor oligomer is modeled by the complex $[Si_3O_6H_5CaHPO_4(H_2O)_3]^-$. The actual precursor is proposed to contain two or three calcium hydrogen phosphate units with a stoichiometry such as $[Si_3O_6H_5CaHPO_4(H_2O)_n]^-$, where $n = 2$ or 3. The complex $[Si_3O_6H_5CaHPO_4(H_2O)_3]^-$, young bone, and bioceramic reacting with simulated body fluid share unique infrared/Raman bands at 631 and 1125−1145 cm^{-1}, which are distinct from the bands observed in crystalline apatite and mature bone. Predicted ^{43}Ca NMR shifts provide avenues for future experiments.

1. Introduction

Bone is a composite material consisting of the mineral dahllite (carbonate-rich hydroxyapatite) and collagen, a protein. Human blood plasma is supersaturated with respect to apatite, but apatite does not precipitate at all sites in the body. Apatite precipitation is promoted only at specific bone-mineralizing sites associated with collagen surfaces. There has been much debate in the literature regarding the role of collagen, and whether a precursor phase such as octacalcium phosphate (OCP; $Ca_8H_2(PO_4)_6{\cdot}5H_2O$) or brushite (dicalcium phosphate dihydrate, DCPD; $CaHPO_4{\cdot}2H_2O$) or poorly crystalline hydroxyapatite (HAP; $Ca_5(PO_4)_3OH$) nucleates apatite precipitation (reviewed in refs 1−4). The small size (1−2 nm) of the earliest mineral deposits in bone has made it difficult to identify the precursor phase, if any, by traditional methods such as X-ray diffraction.

In a related phenomenon, SiO_2-based bioceramics and silica gels promote apatite formation at their surfaces when immersed in simulated body fluids of composition similar to human blood plasma (Table 1). Bioceramic prostheses bond strongly to the existing bone by the formation of a new apatite layer on their surfaces instead of being resorbed or rejected by the body.[5−9] Again, the reaction mechanism of apatite nucleation is not known, although the silanol surface site (Si−OH), dissolved silicon ions, or dissolved silica oligomers have been proposed as catalyzing agents.[10−15] Even amorphous silica phytoliths isolated from bamboo can promote apatite formation.[16,17] It is also found that silica gels that were synthesized from solutions containing poly(ethylene glycol) (PEG) were effective at precipitating apatite,[18,19] whereas gels synthesized in polyacrylamide-containing solutions or organic-free solutions did not promote apatite precipitation.

Different mechanisms have been proposed to explain apatite nucleation at bioceramic surfaces. One mechanism calls for the calcium ion to adsorb at the silanol site with subsequent attachment of the phosphate ion.[10] This reaction pathway will be referred to in this study as scheme 1. In a recent ^{29}Si and ^{31}P NMR study a different mechanism was advanced involving the formation of a direct Si−O−P bond at the bioceramic surface.[20] We will call this pathway scheme 2. Cho et al.[18,19] proposed that some special structure associated with PEG-silica gels is responsible for apatite precipitation, although the structure was not identified by IR or Raman spectroscopy. Thus, there is a need for new approaches to addressing apatite nucleation on bioceramics, in particular, and biomaterials synthesis, in general. As emphasized by Kasemo and Lausmaa,[21] "the bottleneck in biomaterials research today is the great lack of knowledge about molecular scale properties and ... the lack of methods to obtain such information". Very few theoretical or molecular modeling studies have been undertaken in the fields of biomaterials synthesis and biomineralization.[22−24] In the present study, we propose that reaction energies and spectral properties for molecular clusters predicted by theoretical molecular orbital calculations provide a new tool for exploring reaction mechanisms involving biomaterials and biominerals.

* Corresponding author. E-mail: nsahai@glue.umd.edu. Phone: (301) 405-1868. Fax: (301) 314-9121.

10.1021/jp9935889 CCC: $19.00
Published on Web 04/14/2000

The use of molecular clusters for modeling properties ofa crystalline solids and glasses is a widely accepted procedure.[25,26] Note that throughout this paper the term "cluster" will refer to model molecules or ions used in the molecular orbital calculations. These model clusters are distinct from the term clusters as referred to in the homogeneous or heterogeneous nucleation literature. The latter will be distinguished by using qualifying terms such as the nucleating cluster or critical nucleus, subcritical cluster, stable oligomers, etc. In the present study, Si ring clusters are used as models for the bioceramic surfaces, consistent with the proposition that silanol sites are involved in the nucleation of apatite.[10,11,22,23,27] We attempt to determine the reaction pathway for apatite surface nucleation by focusing on questions such as the following: (i) What are the types of calcium and phosphate surface complexes formed at silica surfaces? (ii) What effect does pH have on such interactions? (iii) What are the ^{29}Si, ^{31}P, and ^{43}Ca NMR shieldings of the nuclei in these clusters? (iv) Does a precursor phase nucleate apatite?

The questions posed above refer to chemical species in equilibrium states. Yet, we have set ourselves the task of determining the reaction pathway, which involves identification of transition states. We can circumvent this apparent inconsistency by assuming that the model clusters represent stable intermediates at different stages during the progress of the reaction. Then, by applying Hammond's postulate,[28] we can obtain information about the reaction pathway without actually identifying the transition state. To elaborate, a stable intermediate is a local minimum on a potential energy surface. The distinction between a transition state and a stable intermediate is that the transition state is always in the act of decomposing to reactants or products. An intermediate on the other hand needs further activation for reaction, can in principle undergo a variety of reactions, and is in principle isolatable. There may be an intermediate which has the composition of the activated complex and almost its geometry, and Hammond's postulate[28] relates the degree of correlation one might expect between reaction rates and equilibrium constants: "if two states, as for example, a transition state and an intermediate, occur consecutively during a reaction process and have nearly the same energy content, their interconversion will involve only a small reorganization of the molecular stucture". If clusters are assumed to represent stable intermediates at progressive stages of the reaction, Hammond's postulate suggests that the formation energies of the intermediates will track the energies of the transition states. Thus, our results may be used to interpret the reaction mechanism without actually identifying the activated complex.

2. Computational Details

2.1. Methods. Geometry optimizations and energy calculations for clusters of atoms were carried out using the quantum chemistry software package GAMESS.[30] We optimized geometries at the self-consistent field level using effective core potentials and valence double-ζ basis sets.[31] "Bare" and explicitly hydrated clusters examined included H_3PO_4, $H_2PO_4^-$, HPO_4^{2-}, PO_4^{3-}, $CaHPO_4$, $Ca^{2+}\cdot(H_2O)_6$, $H_2PO_4^-\cdot(H_2O)_4$, $HPO_4^{2-}\cdot(H_2O)_4$, $PO_4^{3-}\cdot(H_2O)_4$, $CaHPO_4\cdot(H_2O)_4$, $CaHPO_4\cdot(H_2O)_8$, $Si(OH)_4$, and $[Si(OH)_3O]^-$. A complete list is provided in Table 2.

The bioceramic silica surface was represented by the silicon 3-ring ($Si_3O_6H_6$), silicon 4-ring ($Si_4O_8H_8$), and a double ring with an open cube structure ($Si_7O_{12}H_{10}$) at various protonation levels: the fully protonated 3-ring and open double ring, $[Si_3O_6H_6]$ and $[Si_7O_{12}H_{10}]$; partially deprotonated 3- and 4- rings and open double rings, $[Si_3O_6H_5]^-$, $[Si_4O_8H_7]^-$, and $[Si_7O_{12}H_9]^-$; and the fully deprotonated 3-ring, $[Si_3O_6H_3]^{3-}$. These structures have been observed in silica glasses and silica gel bioceramics,[32−35] and have been modeled in previous ab initio studies.[23,36] Sorbed calcium ions were represented by clusters such as $[Si_3O_6H_6Ca]^{2+}$ or $[Si_7O_{12}H_{10}Ca]^{2+}$; sorbed calcium phosphates were represented by $[Si_3O_6H_6CaHPO_4]^0$ or $[Si_7O_{12}H_{10}CaHPO_4]^0$, and $[Si_3O_6H_6CaH_2PO_4]^+$ or $[Si_7O_{12}H_{10}CaH_2PO_4]^+$. Explicitly hydrated surfaces were represented by clusters such as $[Si_3O_6H_6(H_2O)_3]^0$ and $[Si_4O_8H_7Ca(H_2O)_6]^+$. The open double ring required prohibitive computational effort so a limited number of calculations were performed and explicit hydration was not considered for all the open double ring clusters. Clusters for scheme 2 were represented by $[Si_3O_6H_5P(OH)O_2(H_2O)_5]^-$, $[Si_3O_6H_5P(OH)O_2Ca(H_2O)_6]^+$, $[Si_3O_6H_5PO_3(H_2O)_5]^{2-}$, and $[Si_3O_6H_5PO_3Ca(H_2O)_6]^0$. Most optimizations were performed without any symmetry constraints except for the fully protonated 3-ring, the fully deprotonated 3-ring, the H_3PO_4 and HPO_4^{2-} clusters where C_{3v} symmetry was imposed, and the H_4SiO_4 cluster where S_4 symmetry was assumed. All geometry-optimized clusters considered in this study are listed in Table 2 with the corresponding energies. Bond lengths for selected clusters are given in Appendix Table A1.

TABLE 1: Compositions (mM) of Human Blood Plasma and Simulated Body Fluids Supersaturated with Respect to Apatite[16]

ion	human blood plasma	simulated body fluid	ion	human blood plasma	simulated body fluid
pH	7.3	7.25	Mg^{2+}	1.5	1.5
Na^+	142.0	142.0	Cl^-	103.0	148.8
K^+	5.0	5.0	HCO_3^-	27.0	4.2
Ca^{2+}	2.5	2.5	HPO_4^{2-}	1.0	1.0

Energies were calculated at the same level of accuracy as the geometry optimizations and vibrational analysis because we were mainly interested in energy trends rather than in absolute values. No corrections were made for electron correlation, basis set truncation error, or basis set superposition error. The use of effective core potentials means that core electrons are ignored and only the energy of the valence electrons is calculated. In this context, the energies of bare cations such as Ca^{2+} and H^+ are calculated as zero because they do not possess any valence electrons. Energies are reported in Table 2. We did not perform normal-mode analysis for all the clusters due to computational limitations imposed by the large cluster sizes, so zero-point energies and entropic contributions to reaction energies were not calculated in most cases. For the few exceptions where we did perform vibrational analyses, the zero-point energies are reported in Table 2.

We have calculated the solvation enthalpy (ΔH_{solv}) for clusters by using the modified Born model of Rashin and Honig,[37] which is a dielectric continuum model. The effective radius was estimated by employing the SCRF "Volume" option in Gaussian 94.[38] The valence double-ζ basis of Stevens et al.[31] is not available in Gaussian 94, so we used another effective core potential implemented in Gaussian 94 as the "LanL2DZ" basis set for the Volume calculations. Solvation enthalpies for selected clusters are reported in Table 3. The combination of explicit waters of hydration to account for short-range hydration forces and the addition of a continuum contribution to account for long-range effects have been used previously by several workers.[39−42]

An estimate of the error in bond lengths may be obtained by comparing P−O bond lengths in the model clusters H_3PO_4 and

TABLE 2: Calculated Gas-Phase Energies (E_{gas}) Using Effective Core Potentials and Valence Double-ζ Basis Sets[a]

cluster	E_{gas} (hartrees)	^{29}Si σ (ppm)	^{31}P σ (ppm)	^{43}Ca σ (ppm)
	Scheme 1			
	3-Ring Clusters			
	Stage 1			
$[Si_3O_6H_6(H_2O)_3]^0$ (C_3v symmetry imposed)	−159.9456	556		
$[Si_3O_6H_5(H_2O)_3]^-$	−159.391(6) (ZPE = 0.154)	564.6 (SiO^-), 555.0, 554.4 (mean 558)		
$[Si_3O_6H_3(H_2O)_3]^{3-}$ (C_3v symmetry imposed)	−157.9902	562		
$[Si_3O_6H_6]^0$ (C_3v symmetry imposed)	−109.3866	557		
$[Si_3O_6H_5]^-$	−108.842(5)	543 (SiO^-), 544		
$[Si_3O_6H_3]^{3-}$ (C_3v symmetry imposed)	−107.3246	559		
	Stage 2			
$[Si_3O_6H_6Ca]^{2+}$	−109.5933	538		1328
$[Si_3O_6H_6Ca(H_2O)_3]^{2+}$	−160.292(8)	538, 538, 540		1264
$[Si_3O_6H_6Ca(H_2O)_6]^{2+}$ (inner-sphere)	−210.902(5)	538, 539, 539		1253
$[Si_3O_6H_6Ca(H_2O)_3\cdots(H_2O)_3]^{2+}$ (hydrated inner-sphere)	−210.81266	539		1315
$[Si_3O_6H_6(H_2O)_3Ca(H_2O)_3]^{2+}$ (outer-sphere)	−211.13(6)	550, 553, 554 (mean 552)		1282
$[Si_3O_6H_6Ca(OH)_3(H_2O)_3]^-$ (surface hydroxide)	−209.6668	555		1250
$[Si_3O_6H_5Ca]^+$	−109.356(7)	534 (SiO^-), 532, 532		1318
$[Si_3O_6H_5Ca(H_2O)_3]^+$	−160.023(1)	543 (SiO^-), 539, 537		1251
$[Si_3O_6H_5Ca(H_2O)_6]^+$ (inner-sphere)	−210.606(1)	542 (SiO^-), 539, 536 (mean 539)		1246
$[Si_3O_6H_5Ca(H_2O)_3\cdots(H_2O)_3]^+$ (hydrated inner-sphere; started out as outer-sphere)	−210.4979(5)	540 (SiO^-), 539, 539		1304
$[Si_3O_6H_3Ca]^-$	−108.4543	538		1262
$[Si_3O_6H_3Ca(H_2O)_3]^-$	−159.099	541		1248
$[Si_3O_6H_3(H_2O)_3\cdots Ca(H_2O)_3]^-$ (hydrated inner-sphere)	−209.54(6)	537		1261
$[Si_3O_6H_3Ca(H_2O)_6]^-$ (inner-sphere)	−209.6566	539		1244
$[Si_3O_6H_6Ca(OH)_3(H_2O)_3]^-$ (hydroxide) (started out as $[Si_3O_6H_3(H_2O)_3Ca(H_2O)_3]^-$)	−209.6668	555		1250
	Stage 3			
$[Si_3O_6H_6CaHPO_4]^0$	−180.0214	539, 539, 541	487	1266
$[Si_3O_6H_6CaH_2PO_4]^+$	−180.4302(7)	540, 541, 541	489	1272
$[Si_3O_6H_6CaHPO_4(H_2O)_3]^0$	−230.65(5)	541, 541, 541	487	1255 (6-31G* value 1222 ppm)
$[Si_3O_6H_6CaH_2PO_4(H_2O)_3]^+$	−231.052(3)	540, 541, 541	484	1269
$[Si_3O_6H_5CaHPO_4]^-$	−179.5424	546, 524, 540	482	1254
$[Si_3O_6H_5CaH_2PO_4]^0$	−180.0641(7)	544.4, 541.7, 540	488	1267
$[Si_3O_6H_5CaHPO_4(H_2O)_3]^-$	−230.16(2) (ZPE 0.1954)	547, 542, 540 (mean 543)	484	1257 (6-31G* value 1218 ppm)
$[Si_3O_6H_5CaH_2PO_4(H_2O)_3]^0$	−230.6623(7)	543, 540, 542	485	1268
$[Si_3O_6H_4CaHPO_4(H_2O)_3]^{2-}$ (started out as $[Si_3O_6H_5CaPO_4(H_2O)_3]^{2-}$	−229.534(5)	542, 545, 548	480	1255
$[Si_3O_6H_3CaHPO_4]^{3-}$ monodentate	−178.1665	543	479	1282
$[Si_3O_6H_3CaH_2PO_4]^{2-}$	−178.9093	542, 541, 542	476	1255
$[Si_3O_6H_3CaHPO_4(H_2O)_3]^{3-}$ monodentate	−228.79(4)	542	484	1266
$[Si_3O_6H_3CaH_2PO_4(H_2O)_3]^{2-}$	−229.515(8)	540	478	1239
	4-Ring Clusters			
$[Si_4O_8H_7(H_2O)_4]^-$	−212.731(9) (ZPE 0.21057)	583.2, 578.3, 584.9, 585.2 (mean 582.9)		
$[Si_4O_8H_7Ca(H_2O)_6]^+$	−247.082(3)	569 (SiO^-), 565, 578, 578 (mean = 572.5)		1275
$[Si_4O_8H_7CaHPO_4(H_2O)_4]^-$	−283.49(5)	558, 581, 567, 564 (mean 567.5)	482	1256
$[Si_4O_{12}H_{10}CaHPO_4]^-$	−278.9(6)			
	Open Double-Ring Clusters			
$[Si_7O_{12}H_{10}]$	−221.59641			
$[Si_7O_{12}H_9]^-$	−221.08(8)			
$[Si_7O_{12}H_9\cdots H_2O]^-$	−237.947(8)			
$[Si_7O_{12}H_9H_2O]^-$	−237.947(8)			
$[Si_7O_{12}H_{10}Ca]^{2+}$	−221.8504			
$[Si_7O_{12}H_{10}CaHPO_4]^0$ tridentate	−292.24(4)			
$[Si_7O_{12}H_{10}CaHPO_4(H_2O)_3]^0$	−342.77(6)			
	Scheme 2			
$[Si_3O_6H_5PO_3(H_2O)_5]^{2-}$	−246.65(3)	557.4 (SiOP), 553.2, 551.8 (mean 554.1)	464.9	
$[Si_3O_6H_5P(OH)O_2(H_2O)_5]^-$	−247.30(3)	563.6 (SiOP), 552.0, 551.2 (mean 555.6)	494.4	
$[Si_3O_6H_5PO_3Ca(H_2O)_6]^0$	−264.320(6)	570.6 (SiOP), 552.9, 557.8 (mean 560.4)	503.5	1262.0 (6-31G* value 1220 ppm)
$[Si_3O_6H_5P(OH)O_2Ca(H_2O)_6]^+$	−264.73(4)	573.3 (SiOP), 552.4, 558.0 (mean 561.2)	509.8	1270.2

TABLE 2 (Continued)

cluster	E_{gas} (hartrees)	^{29}Si σ (ppm)	^{31}P σ (ppm)	^{43}Ca σ (ppm)
	Other Clusters			
H_2O^0	−16.8434			
H^+	0.0000			
Ca^{2+}	0.0000			
$[Ca(H_2O)_6]^{2+}$	−101.4738			
$CaHPO_4^0$	−70.5178		457	1289
$[CaHPO_4(H_2O)_4]^0$	−138.0798		483	1259
$[CaHPO_4(H_2O)_8]^0$	−205.554(1)		484.7	1244.6
H_4SiO_4 (S_4 symmetry imposed)	−69.0567731	572		
$[H_4SiO_4(H_2O)_4]^0$	−136.462(92)	575		
$(OH)_3SiO^-$ (C_1 symmetry)	−68.4830540	562		
$[(OH)_3SiO(H_2O)_4]^-$	−135.941(65)	572		
H_3PO_4 (C_{3v} symmetry imposed)	−70.9902		486	
$[H_3PO_4(H_2O)_4]^0$	−138.408(2)		494	
$H_2PO_4^-$	−69.7105			
$[H_2PO_4(H_2O)_4]^-$	−137.9160		487	
HPO_4^{2-}	−70.4601		468	
$[HPO_4(H_2O)_4]^{2-}$	−137.2503		476	
PO_4^{3-}	−68.7460(7)		464.4	
$[PO_4(H_2O)_4]^{3-}$	−136.394(4)			
TMS ($Si(CH_3)_4$)		507.5		

[a] NMR isotropic shieldings (σ) using the 3-21G* basis set. 1 hartree = 627.6 kcal mol^{-1} = 2626 kJ mol^{-1}.

$H_3PO_4(H_2O)_4$ with the bond lengths in crystals of H_3PO_4[43] and $H_3PO_4 \cdot {}^1/_2(H_2O)$,[44] as shown in Table 4a. In general, the agreement is good, with calculated bond lengths somewhat shorter than the values observed for the crystals. This is expected for the medium-level basis sets and Hartree−Fock method used in the present study.

Vibrational analysis was performed using the valence double-ζ basis of Stevens et al.[31] for only the following clusters: H_3PO_4, HPO_4^{2-}, PO_4^{3-}, $[Si_4O_8H_7(H_2O)_4]^-$, $[Si_3O_6H_6(H_2O)_3]^0$, $[Si_3O_6H_5(H_2O)_3]^-$, and $[Si_3O_6H_5CaHPO_4(H_2O)_3]^-$. Results for the H_3PO_4, HPO_4^{2-}, and PO_4^{3-} clusters are reported in Table 4b along with the experimental values obtained in aqueous solution to determine the magnitude of error in predicted frequencies. The experimental spectrum of H_3PO_4 shows evidence of H-bonding between the (P)OH and H_2O molecules.[45] Therefore, the PO_4^{3-} cluster probably provides the best comparison as H-bond effects may be less pronounced. The ν_4 and ν_3 modes in PO_4^{3-} are overpredicted by about 16−30 cm^{-1}, whereas the ν_1 mode is underpredicted by about 25 cm^{-1}. Note that we have *not* used the 0.9 scaling factor for the calculated frequencies. In fact, a scaling factor of 1.0 may be more suitable for the valence double-ζ basis set.[42] In general, the predicted results are in excellent agreement with experimental values.

^{29}Si, ^{31}P, and ^{43}Ca NMR shieldings (σ) were calculated using the 3-21G* basis[47] with the GIAO method[48] as implemented in Gaussian 94. Shieldings are reported in Table 2. Higher-level 6-31G* basis calculations were not possible during the development of our study because this basis set is not available for calcium in Gaussian 94. Since the original development of this research, we have acquired Gaussian 98[48] which does contain the higher-level 6-31G* basis set for calcium. Therefore, we have performed 6-31G* NMR calculations for a few selected Ca-containing clusters. Comparison of absolute shieldings at 3-21G* and 6-31G* levels showed that 3-21G* shieldings for ^{29}Si and ^{31}P are overpredicted by about ∼50 and ∼60 ppm, respectively (Table 5). A similar comparison in Table 2 yields a difference of about 40 ppm for ^{43}Ca shieldings.

Isotropic shifts are defined as $\sigma_{standard} - \sigma_{sample\ or\ cluster}$, where our standard for ^{29}Si is the tetramethylsilane (TMS) molecule. The calculated shielding for TMS is reported in Table 2. A more positive shift corresponds to decreased shielding. To determine the error in shifts, we compared 3-21G* shifts of model clusters with experimental values (Table 5b). Comparison of the calculated ^{29}Si shift for $[H_3SiO_3(H_2O)_4]^-$ with the experimental value of −71.0 to −71.5 ppm[50−52] yields an error of about 6.5 ppm. Experimental ^{31}P NMR spectra are usually externally referenced to an 85% H_3PO_4 solution. Considering the small amount of water present in the reference, we do not expect the H_3PO_4 to be solvated or dissociated to any appreciable extent. So we believe that the H_3PO_4 cluster is the most appropriate model as the theoretical reference for calculating ^{31}P shifts. We have chosen the ions of phosphoric acid at different protonation levels to estimate our errors in calculating ^{31}P shifts. Measurements of ^{31}P shifts for the ions of phosphoric acid at different protonation levels[53,54] do not report the concentration of the acid in solution. Thus, there appears to be some ambiguity in the literature regarding the extent of hydration of phosphoric acid solutions used for determining ^{31}P NMR shifts at different protonation levels. We have assumed here that the ions of phosphoric acid must be at least partly hydrated in solution, and we have chosen the clusters $H_2PO_4^- \cdot (H_2O)_4$, $HPO_4^{2-} \cdot (H_2O)_4$, and $PO_4^{3-} \cdot (H_2O)_4$ for comparison with experimental results. Table 5b shows ^{31}P shifts calculated relative to H_3PO_4 for different protonation levels of the hydrated anions. The predicted shifts become more positive as the protonation level decreases. This trend is consistent with the trend obtained in aqueous solutions[54] and for phosphate clusters in solid calcium phosphate minerals,[55] but the error in magnitude of the predicted shift increases as the protonation level of the phosphate cluster decreases.

2.2. Interpretation of Calculated Energies. To determine the relative stability of different species at the standard state (and at constant pressure and volume conditions), one needs to predict the Gibbs free energy for the relevant formation reactions

$$\Delta G^\circ_r = \Delta H^\circ_r - T\Delta S^\circ_r \quad (1)$$

where the standard-state enthalpy (ΔH°_r) is the sum of the internal energy at absolute zero (ΔE_r), the zero-point energy (ΔE^{ZP}), and the thermal contributions to ΔH°_r (ΔH^{therm}), and the standard-state entropy of the reaction (ΔS°_r) is the sum of the vibrational, rotational, and translational entropies. The value

TABLE 3: Calculated Solvation Enthalpies (ΔH_{solv})[a]

cluster	r_e (Å)	ΔH_{solv} (hartrees)
$[Ca(H_2O)_6]^{2+}$	3.98	−0.2673
$[PO_4(H_2O)_4]^{3-}$	4.23	−0.5658
$[HPO_4(H_2O)_4]^{2-}$	4.49	−0.2369
$[H_2PO_4(H_2O)_4]^{-}$	4.47	−0.0595
$[(OH)_3SiO(H_2O)_4]^{-}$	4.33	−0.0614
H_2O: $\Delta H°_{solv}$ ($\Delta H°_{vap}$ exptl, Ben Naim and Marcus, 1984)		−0.0142
H^+ (calcd, Tawa et al., 1998)		−0.4259
$[Si_3O_6H_6(H_2O)_3]^0$	4.90	0.0000
$[Si_3O_6H_6(H_2O)_3Ca(H_2O)_3]^{2+}$	4.96	−0.2145
$[Si_3O_6H_6Ca(H_2O)_6]^{2+}$	5.26	−0.2022
$[Si_3O_6H_6CaHPO_4(H_2O)]_3^0$	5.25	0.0000
$[Si_3O_6H_6CaH_2PO_4(H_2O)_3]^{+}$	5.52	−0.0482
$[Si_3O_6H_5(H_2O)_3]^{-}$	5.18	−0.0513
$[Si_3O_6H_5Ca(H_2O)_6]^{+}$	5.13	−0.0518
$[Si_3O_6H_5CaHPO_4(H_2O)_3]^{-}$	4.95	−0.0537
$[Si_3O_6H_5CaH_2PO_4(H_2O)_3]^0$	5.33	0.0000
$[Si_3O_6H_4CaHPO_4(H_2O)_3]^{2-}$	4.99	−0.2132
$[Si_3O_6H_3(H_2O)]_3^{3-}$	4.83	−0.4955
$[Si_3O_6H_6(OH)_3Ca(H_2O)_3]^{-}$	5.26	−0.0506
$[Si_3O_6H_3Ca(H_2O)_6]^{-}$	5.16	−0.0515
$[Si_3O_6H_3CaHPO_4(H_2O)_3]^{3-}$	5.51	−0.4344
$[Si_3O_6H_3CaH_2PO_4(H_2O)_3]^{2-}$	5.15	−0.2066
$[Si_4O_8H_7(H_2O)_4]^{-}$	5.59	−0.0477
$[Si_4O_8H_7Ca(H_2O)_6]^{+}$	5.25	−0.0506
$[Si_4O_8H_7CaHPO_4(H_2O)_4]^{-}$	5.42	−0.0491
$[Si_3O_6H_5P(OH)O_2(H_2O)_5]^{-}$	5.45	−0.0488
$[Si_3O_6H_5PO_3(H_2O)_5]^{2-}$	5.28	−0.2014
$[Si_3O_6H_5PO_3Ca(H_2O)_6]^0$	–	0.0000
$[Si_3O_6H_5P(OH)O_2Ca(H_2O)_6]^{+}$	5.46	−0.0487
Ca^{2+}	2.11	−0.5041
Ca^{2+} (Rashin and Honig, 1985)	1.86	−0.5713
HPO_4^{2-}	3.79	−0.2807
$H_2PO_4^{-}$	3.54	−0.0751
$(OH)_3SiO^{-}$	3.64	−0.0731
$[Si_3O_6H_6]^0$	4.24	0.0000
$[Si_3O_6H_5]^{-}$	4.25	−0.0626
$[Si_3O_6H_3]^{3-}$	4.28	−0.5592
$[Si_3O_6H_6Ca]^{2+}$	4.11	−0.2588
$[Si_3O_6H_6CaHPO_4]^0$	5.00	0.0000
$[Si_3O_6H_6CaH_2PO_4]^{+}$	4.84	−0.0549
$[Si_3O_6H_5Ca]^{+}$	3.75	−0.0709
$[Si_3O_6H_5CaHPO_4]^{-}$	4.42	−0.0602
$[Si_3O_6H_5CaH_2PO_4]^0$	4.87	0.0000
$[Si_3O_6H_3Ca]^{-}$	4.39	−0.0606
$[Si_3O_6H_3CaHPO_4]^{3-}$	5.25	−0.4559
$[Si_3O_6H_3CaH_2PO_4]^{2-}$	4.95	−0.2149

[a] Calculated according to Rashin and Honig's[37] modified Born equation: $\Delta H_{solv} = -166.9z^2/r_e$ kcal mol^{-1}, and using effective radii (r_e) as determined by the SCRF "volume" option and LanL2DZ basis set in Gaussian 94.[38]

of ΔE_r is relatively easly to calculate for gas-phase reactions (ΔE_{gas}). ΔE^{ZP}, ΔH^{therm}, and $\Delta S°_r$ can be obtained by performing a normal-mode analysis on the optimized stationary point geometry. For the very large clusters such as those in the present study, however, a prohibitive computational effort was required, so we did not perform the vibrational analysis for all the clusters. For those clusters where we did do the vibrational analysis, the zero-point energy is found to be negligible compared to the internal energy (see Table 2). It has been noted previously that $\Delta H°_r$ is dominated by the ΔE_r term.[56,57] We expect, therefore, that our reported energies at least provide meaningful estimates of $\Delta H°_r$, and we will assume for gas-phase reactions that $\Delta E_{gas} \approx \Delta H_{gas} \approx \Delta H°_{gas}$. It is recalled that a negative or positive value for a calculated reaction enthalpy suggests that the reaction is exothermic or endothermic *only* at the standard state, and does not necessarily indicate whether the reaction will proceed spontaneously under the ambient conditions.

The above considerations are sufficient for gas-phase reactions. For reactions in solution, solvation energies ($\Delta G°_{solv}$) must be added to the gas-phase $\Delta G°_r$. It is found that a combined approach where energies of explicitly hydrated clusters are corrected for their respective continuum solvation energies provides the best estimate of the "actual" solvation energy (reviewed in ref 58).

Even with these considerations in mind there are still significant sources of uncertainty in estimating solvation energies. First, interfacial reactions such as those considered in the present study must contend with the additional complication of solvation at the surface of the solid. The contribution to the solvation energy from the dielectric constant is given by the $(1/\epsilon) - 1$ term in the Born equation, where ϵ is the dielectric constant of the medium (here, the interfacial region). We have considered the value of the dielectric constant in the interfacial region adjacent to the silica surface to equal the dielectric constant of bulk water (∼80). This is an oversimplification, but even if the interfacial dielectric constant is different by a factor of 10, the error introduced to the calculated solvation energy is only ∼10−15%. Part of this error is mitigated by the inclusion of explicit waters of hydration at the model ring surfaces. The second source of error in the Born model arises from the fact that the solvation energy varies as the square of the charge on the cluster and inversely as the radius. So errors are compounded if the reaction is not iso-Coulombic or if the radii of the species involved in the reaction vary widely as in the case of calcium, phosphate, and water adsorbing on the silica surface. We attempt to mitigate this error as described in the next paragraph. Third, a neutral species such as H_2O is predicted to have a zero solvation energy within the Born model. We know that this cannot be true because water has a nonzero heat of vaporization. For our present purposes, we assumed the experimental $\Delta H°_{vap}$ of water equal to −0.0158 hartree[59] as a measure of its solvation enthalpy. Fourth, the solvation energy of H^+ is difficult to calculate using the Born model because the radius is undefined, so we have adopted the value of Tawa et al.,[60] who used a theoretical approach more accurate than ours to obtain a value of −0.4259 hartree. Many of the problems outlined above are inherent limitations of continuum solvation models common to most theoretical studies of dissolved species. Fifth, despite corrections for solvation energy, in the present study we expect a substantial discrepancy between the absolute values of predicted and experimental reaction energies, because of the cluster representation for surfaces, limited basis set, neglect of electron correlation, and neglect of basis set superposition error. Finally, we note that, even in very high level calculations of small clusters, it is extremely difficult to estimate absolute equilibrium constants (K) because an error of only 1.4 kcal mol^{-1} in predicted $\Delta H°_r$ or 5 cal mol^{-1} deg^{-1} in $\Delta S°_r$ results in an order of magnitude error in K.

To minimize errors in our interpretations, we will only compare isocoulombic reactions or reactions where the relative stability of product species fulfill two criteria: (i) the species are formed at a given protonation level for the silica rings and/or (ii) the product species have the same charge. For instance, we will only compare the relative stability of an inner-sphere or outer-sphere cluster at the $[Si_3O_6H_6]^0$ surface; we will not directly compare the stability of an inner-sphere cluster at the $[Si_3O_6H_6]^0$ surface with the inner-sphere cluster at the $[Si_3O_6H_5]^-$ or $[Si_3O_6H_3]^{3-}$ surfaces. Similarly, for the sorbed calcium phosphates, we will only compare the relative stability of, say, $[Si_3O_6H_5CaHPO_4(H_2O)_3]^-$ with $[Si_3O_6H_5CaH_2PO_4(H_2O)_3]^0$, not with $[Si_3O_6H_6CaHPO_4(H_2O)_3]^0$. An example of applying cri-

TABLE 4.

a. Comparison of Calculated and Experimental Bond Lengths[a]

bond	calculated length	measured length
	H_3PO_4	H_3PO_4
P−O	1.45, 1.58, 1.58, 1.58	1.52, 1.57, 1.57, 1.58
O−H	0.96	
	$H_3PO_4(H_2O)_4$	$H_3PO_4 \cdot {}^1/_2(H_2O)$
P−O	1.46, 1.57, 1.57, 1.59	1.50, 1.55, 1.55, 1.56 (“type A”)
P−O	1.52, 3.89, 3.89, 3.60 (O atoms from H_2O)	1.48, 1.54, 1.55, 1.56 (“type B”)

b. Comparison of Calculated and Experimental Vibrational Frequencies[b]

calculated frequency and mode	measured frequency and mode
PO_4^{3-}	
418.6 ν_2	420 ν_2
600.3 ν_4	567 ν_4
912.5 ν_1	938 ν_1
1035.3 ν_3	1017 ν_3
HPO_4^{2-}	
373.2, 390.5 PO bend	
550.8, 564.8, 574.1 PO bend	
721.3 P−(OH) symm stretch	
1024.2 P−O stretch	
1123.0 P−O stretch	
1231.0, 1260.1 P−O stretch	
4125.1 O−H stretch	
H_3PO_4	
462.0 PO bend	345, 390 P−O bend
514.0 PO bend	500 P−O bend
912.4 symm P−O stretch	885 P−$(OH)_3$ symm stretch
1021.0 P−O stretch	1008 P−O stretch
1120.0 P−$(OH)_3$ stretch?	1066−1074 P$(OH)_3$ degenerate
1163.5 P═O stretch, P−$(OH)_3$?	1165 P═O stretch
1418.5 P−O stretch?	1250 P−O−H in plane deformation
	1780 combination mode
4037.0, 4043.8 O−H stretch	2370, 3000 O−H stretch

[a] Predicted bond lengths (Å) at the Hartree−Fock level using the valence double-ζ basis set for H_3PO_4 (C_{3v} symmetry imposed) and $H_3PO_4(H_2O)_4$ compared to bond lengths observed in crystalline H_3PO_4[43] and crystalline $H_3PO_4 \cdot {}^1/_2(H_2O)$.[44] [b] Predicted IR vibrational frequencies (cm^{-1}) at the Hartree−Fock level using the valence double-ζ basis set for PO_4^{3-}, HPO_4^{2-}, and H_3PO_4. All calculated frequencies are *unscaled*. Comparison with experimentally measured values is shown for H_3PO_4[45] and PO_4^{3-}.[46]

TABLE 5.

a: Basis Size Effects on Calculated ^{29}Si and ^{31}P NMR Isotropic Shieldings (σ): Comparison of the 3-21G* Basis versus the 6-31G* Basis

	^{29}Si σ (ppm)				^{31}P σ (ppm)		
cluster or ion	3-21G*	6-31G*	$\sigma_{3-21G^*} - \sigma_{6-31G^*}$	cluster or ion	3-21G*	6-31G*	$\sigma_{3-21G^*} - \sigma_{6-31G^*}$
TMS $Si(CH_3)_4$	507.5	450.0	57.5	H_3PO_4 (C_{3v} symmetry)	486.1	419.5	66.6
$[Si_3O_6H_3]^{3-}$	558.8	515.7	43.1	$H_3PO_4(H_2O)_4$	493.9	426.0	68.0
$[Si_3O_6H_6]^0$	556.6	505.8	50.8	$H_2PO_4^-$		420.1	
$[Si_3O_6H_6(H_2O)_3]^0$	556.0	505.9	50.2	$[H_2PO_4(H_2O)_4]^-$	487.4	426.4	61.0
$[Si_3O_6H_3Mg]^-$	543.9	493.9	50.0	HPO_4^{2-}	468.3	411.5	56.8
$[[Si_3O_6H_3Mg(H_2O)_3]^-$	548.0	496.5	51.5	$[HPO_4(H_2O)_4]^{2-}$	476.4	419.1	53.3
$[Si_3O_6H_6MgHPO_4]^0$	547.3	493.0	54.3	PO_4^{3-}	464.4	404.6	59.8
$[Si_3O_6H_5CaHPO_4(H_2O)_3]^-$	543.0	496.5	46.5	$[PO_4(H_2O)_4]^{3-}$		416.5	
$[Si_3O_6H_6CaHPO_4(H_2O)_3]^0$	541.0	494.3	46.7	$[Si_3O_6H_6MgHPO_4]^0$	481	417.	64.0
				$[Si_3O_6H_5CaHPO_4(H_2O)_3]^-$	484	418.9	65.1
				$[Si_3O_6H_6CaHPO_4(H_2O)_3]^0$	487	420.7	66.3

b. Error Estimates for ^{29}Si and ^{31}P NMR Shifts (δ, ppm) at the 3-21G* Level[a]

cluster or ion	calculated δ	cluster or ion	experimental δ
$[(OH)_3SiO(H_2O)_4]^-$	−64.5	$[(OH)_3SiO_{(aq)}]^-$	−71.0[b]
H_3PO_4	0.0	H_3PO_4 (85% aqueous solution)	0.0[c]
$[H_2PO_4(H_2O)_4]^-$	−1.3	$[H_2PO_{4(aq)}]^-$	∼1[c]
$[HPO_4(H_2O)_4]^{2-}$	+10.0	$[HPO_{4(aq)}]^{2-}$	∼3[c]
$[PO_4(H_2O)_4]^{3-}$	+15.0	$[PO_{4(aq)}]^{3-}$	∼5[c]

[a] Standards for ^{29}Si and ^{31}P are TMS and H_3PO_4, respectively. [b] References 50−52. [c] Reference 54. Note that the sign convention used by ref 54 for defining the isotropic shift is opposite to the modern sign convention used in the present study.

terion ii will be afforded by comparing the formation energies of $[Si_3O_6H_6Ca(OH)_3(H_2O)_3]^-$ and $[Si_3O_6H_3Ca(H_2O)_6]^-$. We expect, therefore, that our calculations should at least provide meaningful estimates of the *relative* stabilities of different

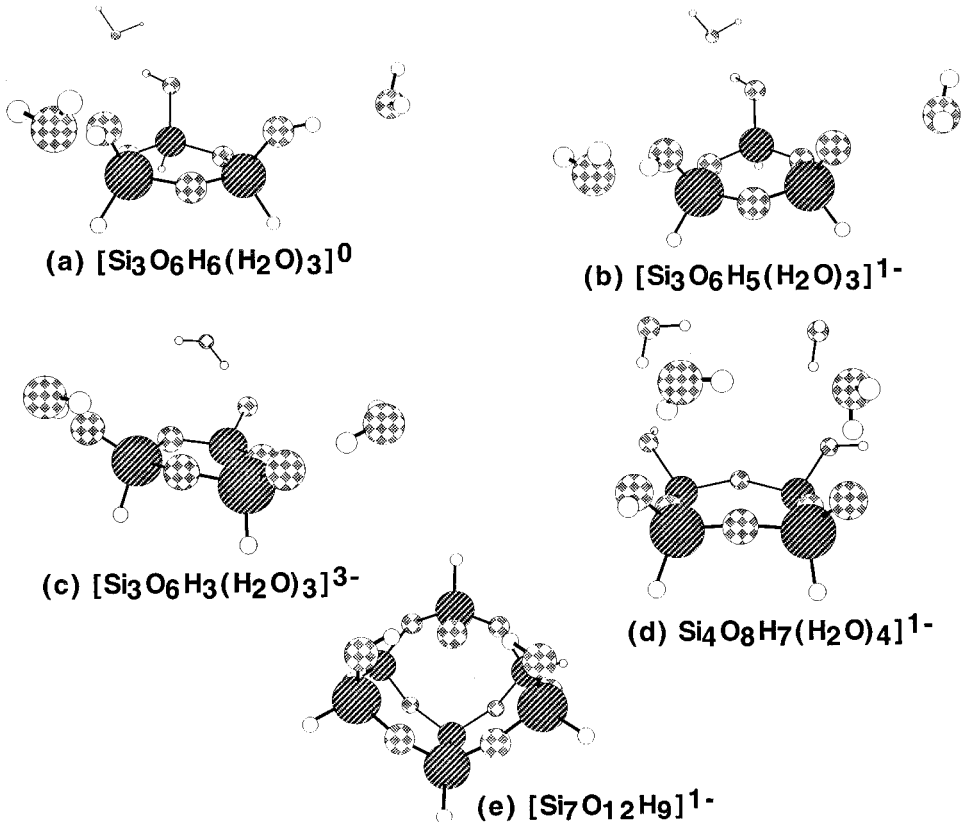

Figure 1. Stage 1 clusters: Model clusters representing reactive (a−d) and average (e) sites on the bioceramic surface. a−c Silicon 3-ring at different protonation levels, $[Si_3O_6H_6(H_2O)_3]^0$, $[Si_3O_6H_5(H_2O)_3]^-$, and $[Si_3O_6H_6(H_2O)_3]^{3-}$. (d) Partially deprotonated Si 4-ring, $[Si_4O_8H_7(H_2O)_4]^-$. (e) $[Si_7O_{12}H_9]^-$. Dark hatched circles: Si. Checkered circles: O. Open circles: H.

species. It should also be remembered that NMR shifts and vibrational frequencies are calculated more reliably then reaction energies, and when compared to experimental shifts, they provide us with additional parameters for basing our interpretations. Finally, note that all the model clusters shown in the figures in this paper were created with the program MacMolplt.[61]

3. Results

3.1. Geometries and Energies.

3.1.1. Scheme 1. Silanol Sites at the Silica Surface (Stage 1). Cluster energies are reported in Table 2 for 3-rings $[Si_3O_6H_6(H_2O)_3]$, $[Si_3O_6H_5(H_2O)_3]^-$, and $[Si_3O_6H_3(H_2O)_3]^{3-}$ (Figure 1a−c), the partially deprotonated 4-ring $[Si_4O_8H_7(H_2O)_4]^-$ (Figure 1d), and the open double-rings $[Si_7O_{12}H_{10}]$ and $[Si_7O_{12}H_9]^-$ (Figure 1e). The Si atoms in the 3-ring and 4-rings are Q^2 species where the superscript "2" indicates that two out of four coordination positions of Si are occupied by a bridging oxygen (O_{br}) that is linked to other Si atoms. The third coordination position is occupied by a terminal silanol ($Si-O_tH$), representing the reacting surface oxygen. To save on computational effort, the 4th coordination position of Si is completed by a terminal H atom instead of an O atom. On a real surface, this last O atom would have connected the Si 3-ring to the underlying bulk of the ceramic.

Calcium Sorption (Stage 2). The addition of a bare calcium ion at all protonation levels of the 3-ring results in bare surface-cation clusters $[Si_3O_6H_6Ca]^{2+}$, $[Si_3O_6H_5Ca]^+$, and $[Si_3O_6H_3Ca]^-$ (not shown). In the case of $[Si_3O_6H_6Ca]^{2+}$ the calcium ion binds to the O_t atoms of the silanol surface groups, and additional bonds are formed with the three Si atoms in $[Si_3O_6H_3Ca]^-$. The calcium ion does not bind to the bridging oxygen atoms (O_{br}) in either the protonated or the deprotonated ring. These geometries, however, do not consider the effects of including explicit waters of hydration.

We increased the degree of hydration of the Ca^{2+} clusters by different methods. In the first method, we started the geometry optimization with an incoming bare calcium ion near the hydrated rings, $[Si_3O_6H_6(H_2O)_3]^0$, $[Si_3O_6H_5(H_2O)_3]^-$, or $[Si_3O_6H_3(H_2O)_3]^{3-}$. In each case, during optimization the three water molecules between the ring and the calcium ion are "pushed out" toward the solution so as to complete the coordination sphere of the metal cation. The calcium ion is moved in toward the ring to form a direct bond with the O_tH or O_t^-, resulting in $[Si_3O_6H_6Ca(H_2O)_3]^{2+}$, $[Si_3O_6H_5Ca(H_2O)_3]^+$, and $[Si_3O_6H_3Ca(H_2O)_3]^-$ (not shown). The calcium ion is now coordinated to the three O_tH molecules or O_t^- ions and the oxygen atoms (O_w) of the water molecules.

In the second method of increasing cluster hydration, we started the optimization with three water molecules between the bare ring $[Si_3O_6H_6]^0$, $[Si_3O_6H_5]^-$, or $[Si_3O_6H_3]^{3-}$ and the incoming calcium ion. Three additional water molecules were introduced "behind" the calcium ion so that it was essentially a hexaquo ion. For $[Si_3O_6H_6]^0$, optimization of the structure did *not* result in the three water molecules between the ring and the calcium ion being pushed out. The resulting structure obtained for the fully protonated ring was $[Si_3O_6H_6(H_2O)_3Ca(H_2O)_3]^{2+}$ (Figure 2a). Three water molecules are about 3 Å away from the terminal silanol oxygens and about 5 Å away from the Si atoms. The calcium ion is about 4.5−4.9 Å from the surface silanol oxygens and ∼5.6 Å from the surface Si atoms. The Ca−O distance in the octahedral hydration sphere of calcium is 2.4 Å. This sort of hydrated surface-cation cluster which has retained its complete primary sheath of hydration and is thus separated from the surface oxygen by at least one

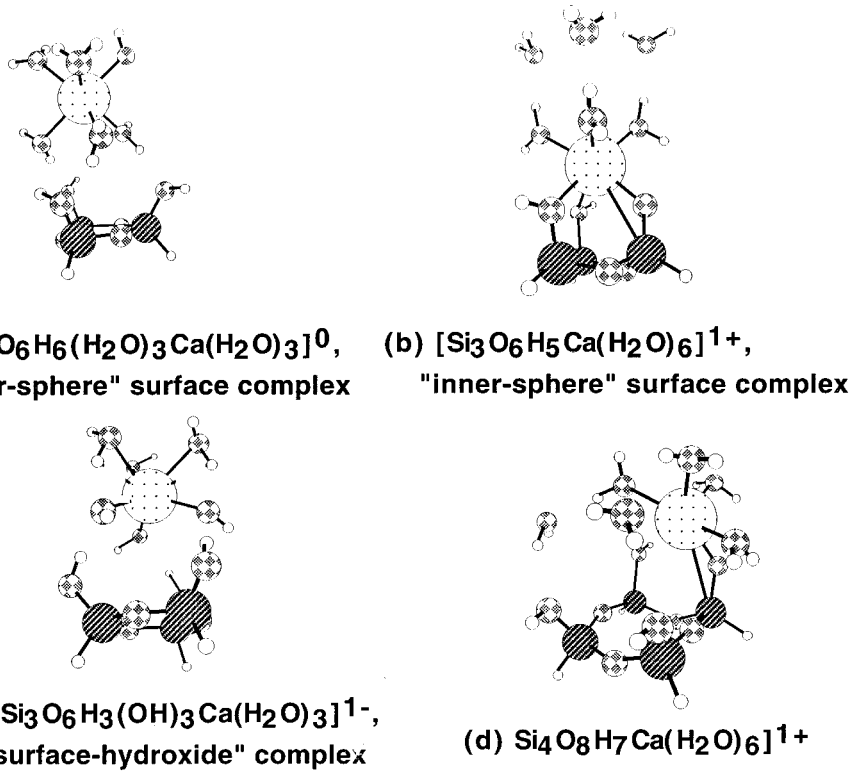

Figure 2. Ca^{2+} sorbed to 3- and 4-rings, representing stage 2 of reaction scheme 1. The calcium ion is explicitly hydrated by six water molecules. The most stable surface complex at each protonation level of the 3-ring is shown. (a) Outer-sphere complex, $[Si_3O_6H_6(H_2O)_3Ca(H_2O)_3]^{2+}$. (b) Inner-sphere complex, $[Si_3O_6H_5Ca(H_2O)_6]^{+}$. (c) Surface hydroxide, $[Si_3O_6H_6(OH)_3Ca(H_2O)_3]^{-}$. (d) $[Si_4O_8H_7Ca(H_2O)_6]^{+}$ represents the inner-sphere complex at the partially deprotonated 4-ring. Compare the different positions of the calcium ion in (a)−(c) versus (d). Dark hatched circles: Si. Checkered circles: O. Open circles: H. Stippled circles: Ca.

layer of water is referred to as an "outer-sphere" surface complex by analogy with aqueous, outer-sphere ion pairs.

We were unable to obtain a stable outer-sphere complex for the $[Si_3O_6H_5]^{-}$ ring. In this case, the three water molecules between the ring and the calcium ion were pushed out, allowing direct bonding of the SiO_t^{-} or SiO_tH sites with calcium, resulting in $[Si_3O_6H_5Ca(H_2O)_3\cdots(H_2O)_3]^{+}$ (not shown). The two water molecules nearest to the calcium were at 4.61 Å, two more were at 5.5 Å, and the last pair of H_2O molecules were even further away at ∼5.9 Å. This optimization indicated the preference of Ca^{2+} to bind directly to the surface oxygens, but the optimized geometry obtained was not octahedral. We have named this cluster "hydrated inner sphere" in Table 2 to distinguish it from the following inner-sphere complex.

We next attempted hydration method 3, to obtain an octahedral inner-sphere complex for Ca^{2+} at the $[Si_3O_6H_5(H_2O)_6]^{+}$ surface. The initial starting geometry consisted of Ca^{2+} near the 3-ring surface with three water molecules behind it corresponding to a partial primary hydration shell, with three more water molecules added further out beyond the primary hydration shell. The outer three water molecules may be considered as forming the secondary solvation sheath of calcium. Thus, the starting geometry was similar to that of the first hydration method described above but included a secondary solvation sheath. In the optimized structure calcium has a coordination number of seven, being bonded to three water molecules, three surface oxygens, and one surface silicon atom. This structure is represented as $[Si_3O_6H_5(H_2O)_6]^{-}$ (Figure 2b). The Ca−O distance to the deprotonated surface oxygen is much shorter (2.09 Å) than the distance to the protonated surface silanols (2.42 and 2.55 Å). The Ca−O distance to the first hydration shell is on average 2.31 Å, whereas the second hydration shell is at a distance of ∼4.61−4.69 Å. We also obtained analogous structures at the other two protonation levels of the 3-ring corresponding to $[Si_3O_6H_6Ca(H_2O)_6]^{2+}$ and $[Si_3O_6H_3Ca(H_2O)_6]^{-}$ (not shown). This sort of surface-cation cluster, where the adsorbed cation has lost part of its primary hydration sheath such that it is directly bonded to the surface oxygen, is referred to as an "inner-sphere" surface complex by analogy with aqueous, contact ion pairs. The use of the terms "inner-sphere" or "outer-sphere" for surface complexes has sometimes led to ambiguity in defining the extent of solvation of the sorbed cation, but the use of these terms is entrenched in the surface-complexation literature, so we will continue their use here.

As with the partially deprotonated 3-ring, our attempt to obtain a stable outer-sphere surface complex, $[Si_3O_6H_3(H_2O)_3Ca(H_2O)_3]^{-}$, was unsuccessful for the totally deprotonated ring, $[Si_3O_6H_3]^{3-}$. One H^{+} from each of the three water molecules between the ring and the $Ca^{2+}(H_2O)_6$ ion was pulled in toward the ring to protonate the O_t^{-} sites, resulting in the "surface hydroxide" $[Si_3O_6H_6(OH)_3Ca(H_2O)_3]^{-}$ geometry (Figure 2c). Thus, the calcium ion is octahedrally coordinated by three hydroxide ions at 2.21 Å and three water molecules at 2.67 Å. The hydroxide ions attached to calcium are at a distance of 2.69 Å from the surface silanol oxygens and 4.65 Å from the surface silicon atoms. The calcium ion is at a distance of 4.11 and 4.65 Å, respectively, from the surface silanol oxygens and the silicon atoms.

Table 6 provides a comparison of reaction energies for the different types of calcium surface complexes described above. If we consider reactions involving $[Si_3O_6H_6(H_2O)_3]$, $Ca^{2+}(H_2O)_6$, and water, the outer-sphere cluster, $[Si_3O_6H_6(H_2O)_3Ca(H_2O)_3]^{2+}$, is more stable than the inner-sphere cluster, $[Si_3O_6H_6Ca(H_2O)_3]^{2+}$. The situation changes as the surface obtains a partial negative charge, i.e., with increasing pH. On

TABLE 6: Calculated Reaction Enthalpies (ΔH_r, hartrees) for Stage 2 of Reaction Schemes 1 and 2[a]

reaction	ΔH_{gas}	ΔH_{solv}	ΔH_r
Scheme 1			
Sorption at $[Si_3O_6H_6]^0$			
$[Si_3O_6H_6(H_2O)_3]^0 + Ca^{2+}(H_2O)_6 = [Si_3O_6H_6(H_2O)_3Ca(H_2O)_3]^{2+}$ (outer-sphere complex) + $3H_2O$	−0.2468	+0.0102	−0.2366
$[Si_3O_6H_6(H_2O)_3]^0 + Ca^{2+}(H_2O)_6 = [Si_3O_6H_6Ca(H_2O)_6]^{2+}$ (inner-sphere complex) + $3H_2O$	−0.0133	+0.0222	+0.0089
Sorption at $[Si_3O_6H_5]^-$			
$[Si_3O_6H_5(H_2O)_3]^- + Ca^{2+}(H_2O)_6 = [Si_3O_6H_5Ca(H_2O)_6]^+$ (inner-sphere complex) + $3H_2O$	−0.2709	+0.2242	−0.0467
Sorption at $[Si_3O_6H_3]^{3-}$			
$[Si_3O_6H_3(H_2O)_3]^{3-} + Ca^{2+}(H_2O)_6 = [Si_3O_6H_3Ca(H_2O)_6]^-$ (inner-sphere complex) + $3H_2O$	−0.7228	+0.6687	−0.0541
$[Si_3O_6H_3]^{3-} + Ca^{2+}(H_2O)_6 = [Si_3O_6H_6(OH)_3Ca(H_2O)_3]^-$ (surface-hydroxide complex or precipitate) + $3H_2O$	−0.733	+0.6696	−0.0634
Sorption at $[Si_4O_8H_7]^-$			
$[Si_4O_8H_7(H_2O)_3]^{3-} + Ca^{2+}(H_2O)_6 = [Si_4O_8H_7Ca(H_2O)_6]^-$ (inner-sphere complex) + $3H_2O$	−0.2502	+0.2076	−0.0426
Scheme 2			
$[Si_3O_6H_6(H_2O)_3]^0 + H_2PO_4^-(H_2O)_4 = [Si_3O_6H_5P(OH)O_2(H_2O)_5]^- + 3H_2O$	+0.028	−0.032	−0.004
$[Si_3O_6H_6(H_2O)_3]^0 + HPO_4^{2-}(H_2O)_4 = [Si_3O_6H_5PO_3(H_2O)_5]^{2-} + 3H_2O$	+0.013	−0.007	+0.006
$[Si_3O_6H_5(H_2O)_3]^- + H_2PO_4^-(H_2O)_4 = [Si_3O_6H_5PO_3(H_2O)5]^{2-} + 3H_2O$	+0.124	−0.133	−0.009
$[Si_3O_6H_5(H_2O)_3]^- + H_2PO_4^-(H_2O)_4 + H^+ = [Si_3O_6H_5P(OH)O_2(H_2O)_5]^- + 3H_2O$	+0.124	+0.293	+0.417

[a] Gas-phase enthalpies (ΔH_{gas}) calculated with effective core potentials and valence double ζ-basis sets.[31] Solvation enthalpy (ΔH_{solv}) from Table 3. $\Delta H_r = \Delta H_{gas} + \Delta H_{solv}$, where we have assumed $\Delta H_{gas} = \Delta E_{gas}$.

TABLE 7: Calculated Reaction Enthalpies (ΔH_r, hartrees) for Stage 3 of Reaction Schemes 1 and 2[a]

reaction	ΔH_{gas}	ΔH_{solv}	ΔH_r
Scheme 1			
$[Si_3O_6H_6(H_2O)_3Ca(H_2O)_3]^{2+} + HPO_4^{2-}(H_2O)_4 = [Si_3O_6H_6CaHPO_4(H_2O)_3]^0 + 7H_2O$	−0.1725	+0.3520	+0.1795
$[Si_3O_6H_6Ca(H_2O)_6]^{2+} + HPO_4^{2-}(H_2O)_4 = [Si_3O_6H_6CaHPO_4(H_2O)_3]^0 + 7H_2O$	−0.406	+0.3397	−0.0663
$[Si_3O_6H_6(H_2O)_3Ca(H_2O)_3]^{2+} + H_2PO_4^-(H_2O)_4 = [Si_3O_6H_6CaH_2PO_4(H_2O)_3]^+ + 7H_2O$	+0.0959	+0.1264	+0.0222
$[Si_3O_6H_6Ca(H_2O)_6]^{2+} + H_2PO_4^-(H_2O)_4 = [Si_3O_6H_6CaH_2PO_4(H_2O)_3]^+ + 7H_2O$	−0.1376	+0.1141	−0.0235
$[Si_3O_6H_5Ca(H_2O)_6]^+ + HPO_4^{2-}(H_2O)_4 = [Si_3O_6H_5CaHPO_4(H_2O)_3]^- + 7H_2O$	−0.2082	+0.1282	−0.0800
$[Si_3O_6H_5Ca(H_2O)_6]^+ + H_2PO_4^-(H_2O)_4 = [Si_3O_6H_5CaH_2PO_4(H_2O)_3]^0 + 7H_2O$	−0.0429	+0.0045	−0.0384
$[Si_3O_6H_3Ca(H_2O)_6]^- + HPO_4^{2-}(H_2O)_4 = [Si_3O_6H_3CaHPO_4(H_2O)_3]^{3-} + 7H_2O$	+0.2091	−0.2454	−0.0363
$[Si_3O_6H_6(OH)_3Ca(H_2O)_3]^- + HPO_4^{2-}(H_2O)_4 = [Si_3O_6H_3CaHPO_4(H_2O)_3]^{3-} + 7H_2O$	+0.2193	−0.2463	−0.027
$[Si_3O_6H_3Ca(H_2O)_6]^- + H_2PO_4^-(H_2O)_4 = [Si_3O_6H_3CaH_2PO_4(H_2O)_3]^{2-} + 7H_2O$	+0.1530	−0.1950	−0.0420
$[Si_3O_6H_6(OH)_3Ca(H_2O)_3]^- + H_2PO_4^-(H_2O)_4 = [Si_3O_6H_3CaH_2PO_4(H_2O)_3]^{2-} + 7H_2O$	+0.1632	−0.1959	−0.0327
$[Si_4O_8H_7Ca(H_2O)_6]^- + HPO_4^{2-}(H_2O)_4 = [Si_4O_8H_7CaHPO_4(H_2O)_4]^- + 6H_2O$			
Scheme 2			
$[Si_3O_6H_5PO_3(H_2O)_5]^{2-} + Ca^{2+}(H_2O)_6 = [Si_3O_6H_5PO_3Ca(H_2O)_6]^0 + 5H_2O$	−0.411	+0.398	−0.013
$[Si_3O_6H_5P(OH)O_2(H_2O)_5]^- + Ca^{2+}(H_2O)_6 = [Si_3O_6H_5P(OH)O_2Ca(H_2O)_6]^+ + 5H_2O$	−0.174	+0.196	+0.022

[a] Gas-phase enthalpies (ΔH_{gas}) calculated with effective core potentials and valence double ζ-basis sets.[31] Solvation enthalpy (ΔH_{solv}) from Table 3. $\Delta H_r = \Delta H_{gas} + \Delta H_{solv}$, where we have assumed $\Delta H_{gas} = \Delta E_{gas}$. Reactions represent sorption of HPO_4^{2-} and HPO_4^- at inner-sphere and outer-sphere calcium surface complexes.

the $[Si_3O_6H_5(H_2O)_3]^-$ surface, the inner-sphere complex was the only stable configuration obtained. Finally, the surface hydroxide, $[Si_3O_6H_6(OH)_3Ca(H_2O)_3]^-$, is more stable than the inner-sphere complex, $[Si_3O_6H_3Ca(H_2O)_6]^-$. The reaction for formation of the hydroxide can be compared consistently with the inner-sphere complex because both products have the same charge. Table 6 also shows that, in general, reactions where the surface complex produced has a smaller absolute charge than the reactant surface are favored relative to the corresponding reactions where the product surface complex has a greater absolute charge than the original reactant surface. For instance, formation of $[Si_3O_6H_3Ca(H_2O)_6]^-$ from $[Si_3O_6H_3(H_2O)_3]^{3-}$ is exothermic, whereas formation of $[Si_3O_6H_6Ca(H_2O)_6]^{2+}$ from $[Si_3O_6H_6(H_2O)_3]^0$ is endothermic.

For the 4-ring, $[Si_4O_8H_7(H_2O)_4]^-$, only a single initial geometry was considered. In the starting geometry, the calcium ion was placed approximately equidistant from all four terminal silanol groups with three water molecules between the ring and the calcium ion, and three more water molecules behind the calcium ion. The optimized geometry is shown in Figure 2d. The intervening water molecules have been pushed out, resulting in an inner-sphere complex with the calcium ion binding preferentially to the deprotonated oxygen and silicon atoms of the silanol group, and to four water molecules. Unlike the 3-ring analogue, the calcium ion is not centered over the ring, but is situated closer to the deprotonated surface oxygen (compare parts b and d of Figure 2).

$H_2PO_4^-$, HPO_4^{2-}, and PO_4^{3-} Sorption (Stage 3). HPO_4^{2-} and $H_2PO_4^-$ were initially introduced to the calcium-sorbed rings in all three protonation levels with three water molecules between the sorbed calcium and the incoming HPO_4^{2-} and $H_2PO_4^-$ groups. During optimization, the three water molecules were pushed out. In the case of $[Si_3O_6H_6CaH_2PO_4(H_2O)_3]^+$ and $[Si_3O_6H_5CaH_2PO_4(H_2O)_3]^0$, one of the water molecules bonded directly to the Ca^{2+} ion while the other two water molecules formed hydrogen bonds with the oxygen atoms of the phosphate cluster as well as with the O_t of the silica ring. $H_2PO_4^-$ attaches to the sorbed calcium at the 3-rings in a bidentate fashion via two O atoms of the PO_4 group. HPO_4^- also sorbs to calcium in a similar bidentate fashion at the fully protonated or partially deprotonated rings, resulting in $[Si_3O_6H_6CaHPO_4(H_2O)_3]^0$ and $[Si_3O_6H_5CaHPO_4(H_2O)_3]^-$. (Figure 3a,b). The bidentate geometry obtained is similar to the local geometry around the Ca^{2+} and phosphate ions in DCPD, OCP, and HAP.[2] However, HPO_4^- attaches to calcium at the fully deprotonated surface via only one oxygen atom, forming a monodentate surface

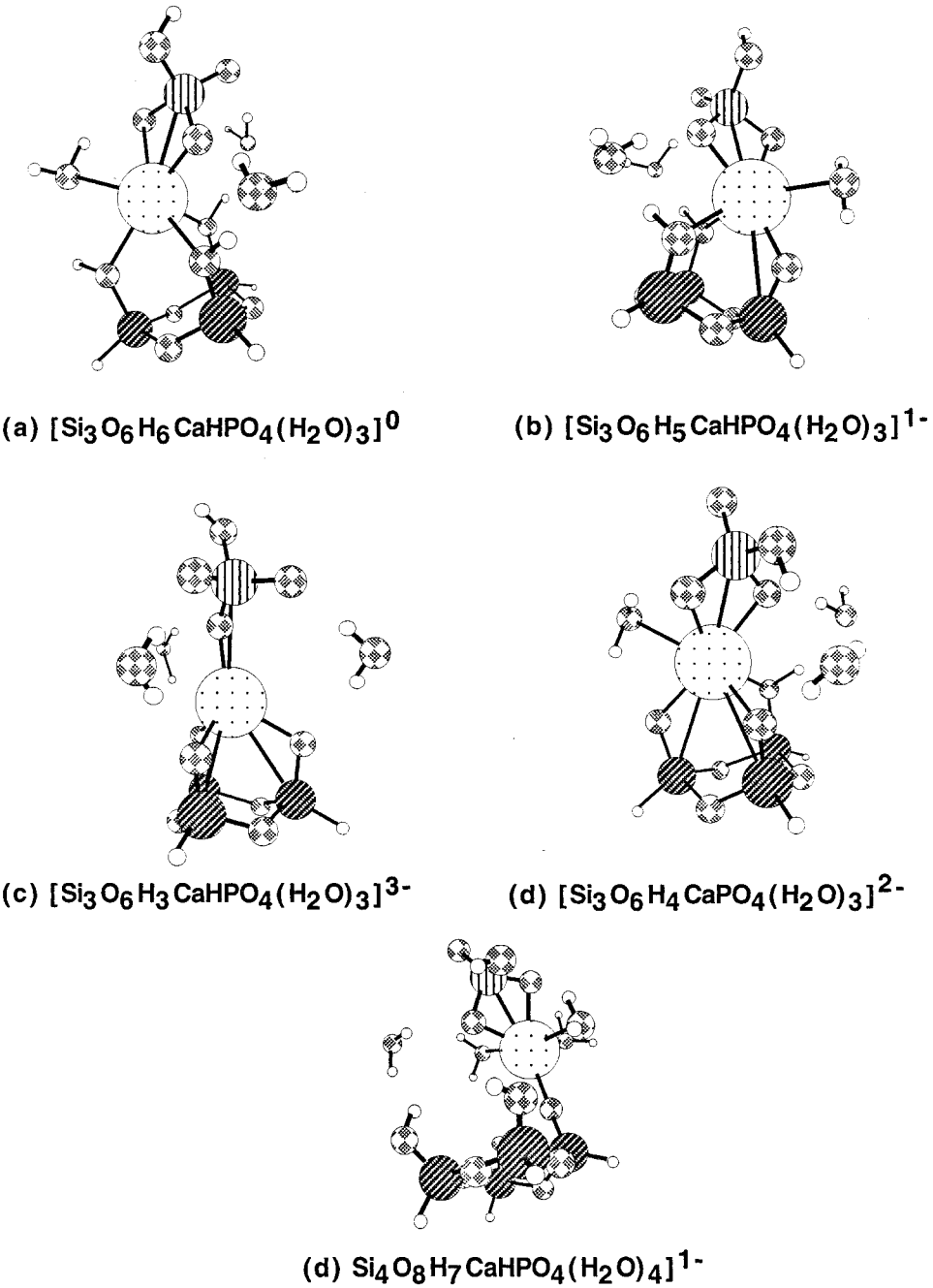

Figure 3. HPO_4^{2-} attached to calcium sorbed on the silicon 3-ring at different protonation levels (a−c), and on the partially deprotonated 4-ring (d), representing stage 3 of reaction scheme 1. The calcium phosphate surface complex is explicitly hydrated by three water molecules (a−c) and by four molecules (d). The most stable surface complex is shown for the fully protonated and partially deprotonated Si 3-rings: (a) $[Si_3O_6H_6CaHPO_4(H_2O)_3]^+$ and (b) $[Si_3O_6H_5CaHPO_4(H_2O)_3]^-$. For the fully deprotonated 3-ring, the less stable, monodentate surface complex $[Si_3O_6H_3(OH)_3CaHPO_4(H_2O)_3]^-$ is shown in (c). Also shown in (d) is $[Si_3O_6H_4CaHPO_4(H_2O)_3]^{2-}$, which started out as $[Si_3O_6H_5CaPO_4(H_2O)_3]^{2-}$. Note in (e) ($[Si_4O_8H_7CaHPO_4(H_2O)_4]^-$), the different position of the $CaHPO_4$ moiety compared to those in (a)−(d). Dark hatched circles: Si. Checkered circles: O. Open circles: H. Stippled circles: Ca. Light hatched circles: P.

complex, forming $[Si_3O_6H_3CaHPO_4(H_2O)_3]^{3-}$ (Figure 3c). These results show that the geometry of the surface complex depends on the protonation level of both the surface and the phosphate group.

Energies for formation of stage 3 clusters from stage 2 clusters are reported in Table 7. The formation energies of hydrated surface complexes from hydrated reactants are shown in Table 8. At the two higher protonation levels, where bidentate clusters are formed with both HPO_4^{2-} and $H_2PO_4^-$, the surface complexes involving HPO_4^{2-} are more stable. For the completely deprotonated surface, however, a comparison of reaction energies indicates that the bidentate cluster involving $H_2PO_4^-$, i.e., $[Si_3O_6H_3CaH_2PO_4(H_2O)_3]^{2-}$, is more stable than the monodentate cluster involving HPO_4^{2-}, i.e., $[Si_3O_6H_3CaHPO_4(H_2O)_3]^{3-}$ (Table 8).

Finally, PO_4^{3-} was introduced to $[Si_3O_6H_5Ca(H_2O)_3]^+$ and $[Si_3O_6H_6Ca(H_2O)_3]^{2+}$ clusters so that the starting clusters had the stoichiometries, $[Si_3O_6H_5CaPO_4(H_2O)_3]^{2-}$ and $[Si_3O_6H_6CaPO_4(H_2O)_3]^-$, respectively. During optimization, one H atom from a terminal silanol group on the ring was abstracted by the PO_4^{3-}, resulting in clusters represented by $[Si_3O_6H_4CaHPO_4(H_2O)_3]^{2-}$ (Figure 3d) and $[Si_3O_6H_5CaHPO_4(H_2O)_3]^-$, respec-

TABLE 8: Overall Reaction Enthalpies (ΔH_r, hartrees) for Ca^{2+}, $H_2PO_4^-$, HPO_4^{2-}, and PO_4^{3-} Bonding to the Silica Surface According to Schemes 1 and 2[a]

reaction	ΔH_{gas}	ΔH_{solv}	ΔH_r
Scheme 1			
$[Si_3O_6H_6(H_2O)_3]^0 + Ca^{2+}(H_2O)_6 + H_2PO_4^-(H_2O)_4 = [Si_3O_6H_6CaH_2PO_4(H_2O)_3]^+ + 10H_2O$	−0.1509	+0.1366	−0.0143
$[Si_3O_6H_6(H_2O)_3]^0 + Ca^{2+}(H_2O)_6 + HPO_4^{2-}(H_2O)_4 = [Si_3O_6H_6CaHPO_4(H_2O)_3]^0 + 10H_2O$	−0.4188	+0.3622	−0.0571
$[Si_3O_6H_5(H_2O)_3]^- + Ca^{2+}(H_2O)_6 + H_2PO_4^-(H_2O)_4 = [Si_3O_6H_5CaH_2PO_4(H_2O)_3]^0 + 10H_2O$	−0.3150	+0.2351	−0.0799
$[Si_3O_6H_5(H_2O)_3]^- + Ca^{2+}(H_2O)_6 + HPO_4^{2-}(H_2O)_4 = [Si_3O_6H_5CaHPO_4(H_2O)_3]^- + 10H_2O$	−0.4803	+0.3596	−0.1307
$[Si_3O_6H_5(H_2O)_3]^- + Ca^{2+}(H_2O)_6 + PO_4^{3-}(H_2O)_4 = [Si_3O_6H_4CaHPO_4(H_2O)_3]^{2-} + 10H_2O$	−0.7087	−0.5292	−0.1795
$[Si_3O_6H_3(H_2O)_3]^{3-} + Ca^{2+}(H_2O)_6 + H_2PO_4^-(H_2O)_4 = [Si_3O_6H_3CaH_2PO_4(H_2O)_3]^{2-} + 10H_2O$	−0.5698	+0.4738	−0.0960
$[Si_3O_6H_3(H_2O)_3]^{3-} + Ca^{2+}(H_2O)_6 + HPO_4^{2-}(H_2O)_4 = [Si_3O_6H_3CaHPO_4(H_2O)_3]^{3-} + 10H_2O$	−0.5137	+0.4233	−0.0904
$[Si_4O_8H_7(H_2O)_3]^- + Ca^{2+}(H_2O)_6 + HPO_4^{2-}(H_2O)_4 = [Si_4O_8H_7CaHPO_4(H_2O)_3]^0 + 10H_2O$	−0.473	+0.3608	−0.1122
Scheme 2			
$[Si_3O_6H_6(H_2O)_3]^0 + Ca^{2+}(H_2O)_6 + H_2PO_4^-(H_2O)_4 = [Si_3O_6H_5P(OH)O_2Ca(H_2O)_6]^+ + 8H_2O$	−0.146	+0.165	+0.019
$[Si_3O_6H_6(H_2O)_3]^0 + Ca^{2+}(H_2O)_6 + HPO_4^{2-}(H_2O)_4 = [Si_3O_6H_5PO_3Ca(H_2O)_6]^0 + 8H_2O$	−0.398	+0.391	−0.008
$[Si_3O_6H_5(H_2O)_3]^- + Ca^{2+}(H_2O)_6 + H_2PO_4^-(H_2O)_4 + H^+ = [Si_3O_6H_5P(OH)O_2Ca(H_2O)_6]^+ + 8H_2O$	−0.2864	+0.6904	+0.404
$[Si_3O_6H_5(H_2O)_3]^- + Ca^{2+}(H_2O)_6 + + H_2PO_4^-(H_2O)_4 = [Si_3O_6H_5PO_3Ca(H_2O)_6]^0 + 8H_2O$	−0.2864	+0.2645	−0.0199

[a] Gas-phase enthalpies (ΔH_{gas}) calculated with effective core potentials and valence double ζ-basis sets.[31] Solvation enthalpy (ΔH_{solv}) from Table 3. $\Delta H_r = \Delta H_{gas} + \Delta H_{solv}$, where we have assumed $\Delta H_{gas} = \Delta E_{gas}$.

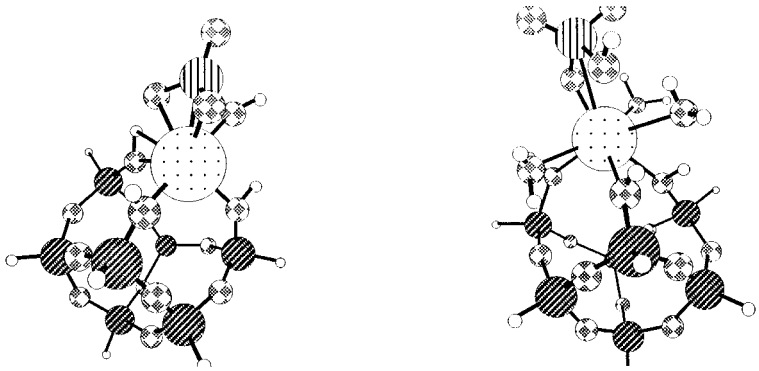

Figure 4. Ca^{2+} or Mg^{2+} and HPO_4^{2-} sorbed to the open double ring: (a) nonhydrated, tridentate cluster $[Si_7O_{12}H_{10}CaHPO_4]^0$, (b) hydrated, bidentate cluster, $[Si_7O_{12}H_{10}CaHPO_4(H_2O)_3]^0$. Note the difference in geometries obtained. Dark hatched circles: Si. Checkered circles: O. Open circles: H. Stippled circles: Ca. Light hatched circles: P.

tively. Thus, the appropriate protonation level for the phosphate group appears to be HPO_4^{2-}.

For the 4-ring, we optimized only the complex involving HPO_4^{2-}. The resulting structure, $[Si_4O_8H_7CaHPO_4(H_2O)_4]^-$, is shown in Figure 3e. The calcium ion continues to be attached to the Si ring at only one SiO^- site, and the HPO_4^{2-} has sorbed to the calcium by bidentate bonds.

Effects of Model Cluster Size. The behavior of calcium phosphate sorbed to the open double ring is different from that for the 3-ring and the 4-ring in several respects. First, HPO_4^{2-} attaches to calcium on the open double ring in tridentate fashion, forming $[Si_7O_{12}H_{10}CaHPO_4]^0$ (Figure 4a). This is different from the bidentate geometry obtained for the corresponding Si 3-ring $[Si_3O_6H_6CaHPO_4]^0$. Second, the introduction of three water molecules to $[Si_7O_{12}H_{10}CaHPO_4]^0$, resulting in $[Si_7O_{12}H_{10}CaHPO_4(H_2O)_3]^0$ (Figure 4b), changes the bond arrangement between Ca^{2+} and HPO_4^{2-} (Figure 4b). The optimized structure obtained in the presence of water, $[Si_7O_{12}H_{10}CaHPO_4(H_2O)_3]^0$, has a monodentate bond between Ca^{2+} and HPO_4^{2-} compared to the preferred bidentate bonds seen in $[Si_3O_6H_6CaHPO_4(H_2O)_3]^0$, $[Si_3O_6H_5CaHPO_4(H_2O)_3]^-$, and $[Si_4O_8H_7CaHPO_4(H_2O)_3]^-$. The calcium ion is coordinated by seven oxygen atoms in $[Si_7O_{12}H_{10}CaHPO_4(H_2O)_3]^0$, including three H_2O molecules, three surface silanol oxygens, and one oxygen from the HPO_4^{2-} ion. Thus, the addition of water affects geometry in the case of the open double ring but not in the case of the 3-ring.

3.1.2. Scheme 2. According to scheme 2a, the $H_2PO_4^-$ or HPO_4^{2-} anion bonds directly to a terminal silanol on the bioceramic surface. We have represented the surface site by the 3-ring at two protonation levels, $[Si_3O_6H_6(H_2O)_3]^0$ and $[Si_3O_6H_5(H_2O)_3]^-$. Sorption of $H_2PO_4^-$ or HPO_4^{2-} at either of these surfaces is predicted to be endothermic or thermoneutral (no change in enthalpy) within error. The clusters formed are $[Si_3O_6H_5P(OH)O_2(H_2O)_5]^-$ and $[Si_3O_6H_5PO_3(H_2O)_5]^{2-}$ (Figure 5a,b). Subsequent sorption of calcium results in $[Si_3O_6H_5P(OH)O_2Ca(H_2O)_6]^+$ and $[Si_3O_6H_5PO_3Ca(H_2O)_6]^0$ (Figure 5 c,d). Of the four reactions considered in Table 8, two are predicted to be endothermic, and one is almost thermoneutral ($\Delta H = 0.008$). Only the formation of $[Si_3O_6H_5PO_3Ca(H_2O)_6]^0$ and eight water molecules from $[Si_3O_6H_5(H_2O)_3]^-$, $H_2PO_4^{1-}(H_2O)_4$, and $Ca^{2+}(H_2O)_6$ (Table 8) is predicted to be exothermic.

3.2. ^{29}Si, ^{31}P, and ^{43}Ca NMR Shieldings. *3.2.1. ^{29}Si Shielding Trends with Reaction Progress.* The hydrated silica ring and the hydrated cation-sorbed ring are relatively more shielded than the corresponding nonhydrated clusters. However, the presence of water slightly *deshields* the ^{29}Si nucleus in the final stage 3

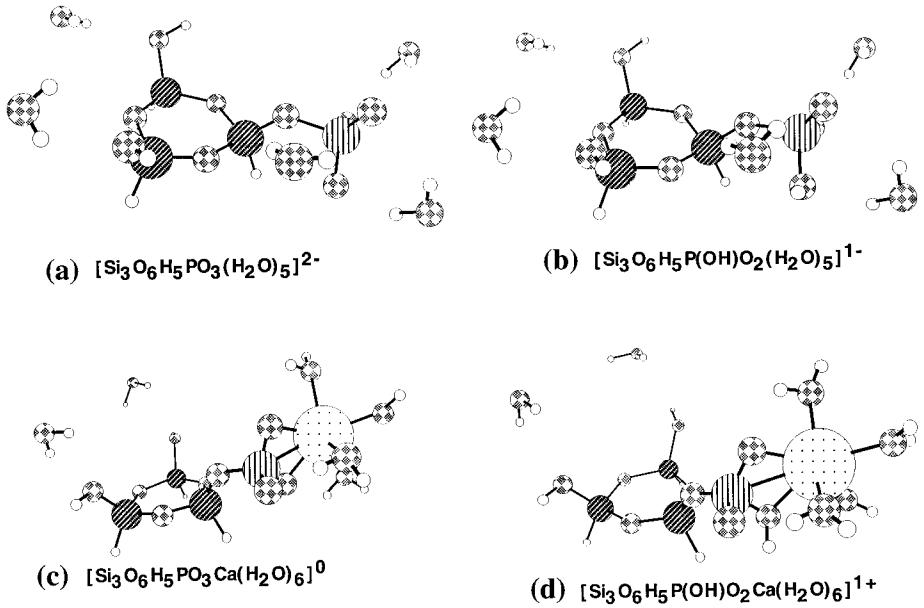

Figure 5. Clusters representing stages 2 and 3 of reaction scheme 2: (a) $[Si_3O_6H_5PO_3(H_2O)_5]^{2-}$, (b) $[Si_3O_6H_5P(OH)O_2(H_2O)_5]^{-}$, (c) $[Si_3O_6H_5PO_3Ca(H_2O)_6]^{0}$, and (d) $[Si_3O_6H_5P(OH)O_2(H_2O)_6]^{+}$. Dark hatched circles: Si. Checkered circles: O. Open circles: H. Stippled circles: Ca. Light hatched circles: P.

TABLE 9: Change (Δ) in Average Calculated ^{29}Si Isotropic Shieldings between Stage 1 and Stage 2 and between Stage 2 and Stage 3 of Reaction Schemes 1 and Scheme 2

stage 1 cluster	stage 2 cluster	^{29}Si Δ, ppm	stage 3 cluster	^{29}Si Δ, ppm
		Scheme 1		
	$[Si_3O_6H_6Ca(H_2O)_6]^{2+}$	−18	$[Si_3O_6H_6CaHPO_4(H_2O)_3]^{0}$	+2.6
$[Si_3O_6H_6(H_2O)_3]^{0}$			$[Si_3O_6H_6CaH_2PO_4(H_2O)_3]^{+}$	+2.4
	$[Si_3O_6H_6(H_2O)_3Ca\ (H_2O)_3]^{2+}$	−4.0	$[Si_3O_6H_6CaHPO_4(H_2O)_3]^{0}$	−11
			$[Si_3O_6H_6CaH_2PO_4(H_2O)_3]^{+}$	−11
$[Si_3O_6H_5(H_2O)_3]^{-}$	$[Si_3O_6H_5Ca(H_2O)_6]^{+}$	−20	$[Si_3O_6H_5CaHPO_4(H_2O)_3]^{-}$	+4.0
			$[Si_3O_6H_5CaH_2PO_4(H_2O)_3]^{0}$	+2.3
	$[Si_3O_6H_3Ca(H_2O)_6]^{-}$	−22	$[Si_3O_6H_3CaHPO_4(H_2O)_3]^{3-}$	+2.6
$[Si_3O_6H_3(H_2O)_3]^{3-}$			$[Si_3O_6H_3CaH_2PO_4(H_2O)_3]^{2-}$	+0.7
	$[Si_3O_6H_6Ca(OH)_3(H_2O)_3]^{-}$	−6.0	$[Si_3O_6H_3CaHPO_4(H_2O)_3]^{3-}$	−13
			$[Si_3O_6H_3CaH_2PO_4(H_2O)_3]^{2-}$	−15
$[Si_4O_8H_7(H_2O)_3]^{-}$	$[Si_4O_8H_7Ca(H_2O)_6]^{+}$	−10	$[Si_4O_8H_7CaHPO_4(H_2O)_3]^{-}$	−5.0
		Scheme 2		
$[Si_3O_6H_6(H_2O)_3]^{0}$	$[Si_3O_6H_5P(OH)O_2(H_2O)_5]^{-}$	−0.4 (+7.6)[a]	$[Si_3O_6H_5P(OH)O_2Ca(H_2O)_6]^{+}$	+5.6 (+9.7)
$[Si_3O_6H_6(H_2O)_3]^{0}$	$[Si_3O_6H_5PO_3(H_2O)_5]^{2-}$	−1.9 (+1.4)[a]	$[Si_3O_6H_5P(OH)O_2Ca(H_2O)_6]^{+}$	+7.1 (+15.9)
$[Si_3O_6H_5(H_2O)_3]^{-}$	$[Si_3O_6H_5P(OH)O_2(H_2O)_5]^{-}$	−3.9 (−7.2)[a]	$[Si_3O_6H_5P(OH)O_2Ca(H_2O)_6]^{+}$	+6.3 (+13.2)
$[Si_3O_6H_5(H_2O)_3]^{-}$	$[Si_3O_6H_5PO_3(H_2O)_5]^{0}$	−2.4 (−1.0)[a]	$[Si_3O_6H_5PO_3Ca(H_2O)_6]^{0}$	+4.8 (+7.0)

[a] Values in parentheses for Scheme 2 refer to changes in ^{29}Si shieldings for the individual Si atom involved in the direct Si−O−P bond.

surface complex. The protonation level of the phosphate cluster does not significantly affect the results (Table 2).

Changes in ^{29}Si shielding of explicitly hydrated Si 3-ring clusters as the reaction progresses are reported in Table 9. At each protonation level of the 3-ring, the pathways involving the inner-sphere calcium complexes yield initially negative changes in shielding, followed by positive changes. For each of these cases, the ^{29}Si nucleus is significantly deshielded by about 18−20 ppm, in going from stage 1 to stage 2. The predicted magnitude of the deshielding is much larger than the ∼2−8 ppm deshielding observed experimentally,[20] but the direction of these changes is consistent with experiment. Stage 2 to stage 3 represented by attachment of the phosphate group to the calcium-sorbed rings results in almost no change (+0.7 ppm) or reverses this trend slightly with a small increase in shielding (+4 ppm) similar to the experimentally observed range of ∼0.4−6.6 ppm. Reactions involving the outer-sphere calcium complex or the surface hydroxide sorbed on the 3-ring show monotonically decreasing shielding from stage 1 through stage 3. Similarly, for the cluster involving the Si 4-ring, the ^{29}Si nucleus is predicted to be deshielded at both stages 2 and 3. These changes in ^{29}Si shielding are not consistent with the trends observed for bioceramic reacting with simulated body fluids.

The ^{29}Si NMR shifts for scheme 2 as the reaction progresses are also summarized in Table 9. For those reaction sequences where stage 1 is $[Si_3O_6H_6(H_2O)_3]^{0}$, the trends in *average* ^{29}Si shieldings are consistent with the experimentally observed changes. The *individual* Si atom involved in the direct Si−O−P bond, however, is more shielded than in the original $[Si_3O_6H_6(H_2O)_3]^{0}$ cluster contrary to the explanation offered by Hayakawa et al. for their own experimental results. Scheme 2 pathways involving $[Si_3O_6H_5(H_2O)_3]^{-}$ in stage 1 have predicted ^{29}Si trends consistent with experimental observation on average as well as for the individual Si atom involved in the Si−O−P bond.

3.2.2. ^{31}P Isotropic and Anisotropic Shifts. Recently, NMR studies of bone compared to calcium orthophosphate minerals have succeeded in identifying a protonated phosphate group that

TABLE 10: 3-21G* ^{31}P Isotropic (σ_{iso}) and Anisotropic Shifts (σ_{aniso}) Calculated for Stage 3 Clusters Compared to Shifts Measured for Calcium Orthophosphate Minerals and Bone[64] [a]

cluster, mineral,[b] or bone[b]	3-21G* (6-31G*) ^{31}P σ_{iso}	3-21G* (6-31G*) ^{31}P σ_{aniso}
Scheme 1 Clusters		
$[Si_3O_6H_6CaHPO_4(H_2O)_3]^0$	−0.9 (−1.2)	112 (116.4)
$[Si_3O_6H_6CaH_2PO_4(H_2O)_3]^+$	+2.0	178
$[Si_3O_6H_5CaHPO_4(H_2O)_3]^-$	+2.0 (+0.6)	107 (112.6)
$[Si_3O_6H_5CaH_2PO_4(H_2O)_3]^0$	+0.7	115
$[Si_3O_6H_3CaHPO_4(H_2O)_3]^{3-}$	+2.0	130
$[Si_3O_6H_3CaH_2PO_4(H_2O)_3]^{2-}$	+8.0	248
$[Si_3O_6H_3CaHPO_4(H_2O)_3]^{3-}$	+2.0	130
$[Si_3O_6H_3CaH_2PO_4(H_2O)_3]^{2-}$	+8.0	248
$[Si_4O_8H_7CaHPO_4(H_2O)_3]^-$	+4.0	158
Scheme 2 Clusters		
$[Si_3O_6H_5PO_3Ca(H_2O)_6]^0$	−21.1 (−0.2)	146 (137.8)
$[Si_3O_6H_5P(OH)O_2Ca(H_2O)_6]^+$	−23.8	224
Orthophosphate Minerals		
DCPD, HPO_4^{2-}	1.4	121
OCP, HPO_4^{2-}	−0.5	65
OCP, PO_4^{3-}	2.8	38
HAP, PO_4^{3-}	2.8	40
CO_3^{2-}−HAP, PO_4^{3-}	2.8	
ACP (amorphous calcium phosphate), PO_4^{3-}	2.8	
β-TCP (tricalcium phosphate), PO_4^{3-}	1.5, 4.3	
Bone		
young bone[c]	−0.1, −0.5	104−116
mature bone[c]	−0.1, −0.5	128

[a] 6-31G* shifts calculated for selected clusters are shown in parentheses. All shifts calculated relative to model cluster H_3PO_4. [b] Reference 63. $\sigma_{aniso} = \sigma_{33} - \sigma_{11}$. [c] We are reporting the range of values obtained by ref 64 for bones of different maturities and from different animals (chick, calf, rabbit).

has spectral properties intermediate to those of HAP, DCPD, and OCP.[62−64] A ^{31}P NMR study on chicken, cow, and rabbit bone showed that the isotropic ^{31}P shift of HPO_4^{2-} in bone was similar to that of OCP (equal to ∼−0.5 ppm) but the anisotropic shift was similar to that of brushite (∼104−128 ppm). Note that the anisotropic shift was defined somewhat unconventionally as the magnitude of the difference between the maximum and minimum eigenvalues of the shielding tensor, σ_{33} and σ_{11}.[64] Using the calculated absolute shielding of H_3PO_4 as the theoretical standard, we obtain isotropic and anisotropic shifts similar to those of bone for $[Si_3O_6H_6CaHPO_4(H_2O)_3]^0$, $[Si_3O_6H_5CaHPO_4(H_2O)_3]^-$, $[Si_3O_6H_5CaH_2PO_4(H_2O)_3]^0$, and $[Si_3O_6H_3CaHPO_4(H_2O)_3]^{3-}$ (Table 10), with both the 3-21G* and the 6-31G* basis sets. The anisotropic shifts for the 4-ring cluster, $[Si_4O_8H_7CaHPO_4(H_2O)_4]^-$, is 158 ppm, quite different from the value for bone or orthophosphate minerals (Table 10). Finally, for scheme 2 clusters, $[Si_3O_6H_5PO_3Ca(H_2O)_6]^0$ and $[Si_3O_6H_5P(OH)O_2Ca(H_2O)_3]^+$, the predicted ^{31}P isotropic shifts using the 3-21G* basis set are −21 and −23.8 ppm, and the anisotropic shifts are 146 and 224.4 ppm, respectively (Table 10). These values are quite different from the values expected for bone and for orthophosphate minerals, although the situation improves somewhat when 6-31G* values are compared to the experimental values.

3.2.3. ^{43}Ca Shielding. Table 2 lists the shieldings calculated using the 3-21G* basis set. Values in parentheses for the clusters $[Si_3O_6H_6CaHPO_4(H_2O)_3]^0$, $[Si_3O_6H_5CaHPO_4(H_2O)_3]^-$, and $[Si_3O_6H_5PO_3Ca(H_2O)_6]^0$ refer to calculations at the higher-level 6-31G* basis set. A comparison shows a fairly constant difference of about 40 ppm between the two basis sets. We can also look at trends in ^{43}Ca shielding with reaction progress. If scheme 1 is the correct reaction sequence, the ^{43}Ca nucleus would be sensitive to both the Si and the P in the next-nearest-neighbor positions. If scheme 2 is the appropriate sequence, then the ^{43}Ca nucleus would not be affected significantly by the Si atom. Thus, in the present system, the NMR shifts of the ^{43}Ca nucleus would probably provide the most useful information on the nature of the bonds formed. The ^{43}Ca nucleus is deshielded by about 138−126 ppm in going from the outer-sphere complex $[Si_3O_6H_6(H_2O)_3Ca(H_2O)_3]^{2+}$ to the $[Si_3O_6H_6CaHPO_4(H_2O)_3]^0$ and $[Si_3O_6H_6CaH_2PO_4\ (H_2O)_3]^+$ complexes (Table 2). For the partially deprotonated ring, the shielding of the ^{43}Ca nucleus is predicted to increase by about 10−12 ppm on going from the inner-sphere $[Si_3O_6H_5Ca(H_2O)_3]^+$ to the hydrated sorbed calcium phosphates. Unfortunately, ^{43}Ca has a 7/2 spin and low-resonance frequency, making experimental spectroscopy difficult. The importance of calcium in the human body has, however, prompted considerable efforts to make ^{43}Ca NMR experimentally more feasible, and such a study has been reported in the biomedical literature.[65] Perhaps, in the future, the predicted ^{43}Ca shieldings can be used for comparison with measured shifts as an additional constraint in apatite nucleation studies.

3.3.Vibrational Analysis. The results shown in Tables 6−10 suggest that, at pH ≈7.3, the $[Si_3O_6H_6CaHPO_4(H_2O)_3]^0$ and $[Si_3O_6H_5CaHPO_4(H_2O)_3]^-$ clusters are the most likely surface complexes at the Si 3-ring surface, so we selected $[Si_3O_6H_6(H_2O)_3]^0$, $[Si_3O_6H_5(H_2O)_3]^-$, and $[Si_3O_6H_5CaHPO_4(H_2O)_3]^-$ for performing vibrational analysis. The calculated normal modes of vibration are shown in Table 11. Many of the modes predicted for $[Si_3O_6H_5CaHPO_4(H_2O)_3]^-$ are combination modes of the Si 3-ring, HPO_4^{2-}, and H_2O vibrations. This makes peak assignment difficult. Therefore, the assignments made for the model clusters refer to the *dominant* mode of vibration. Also shown in Table 11 are the IR spectra measured for some calcium phosphate minerals, for young bone and enamel, and for mature bone.[66−71] The assignments for the experimental spectra shown in Table 11 are as reported in the original sources. Modes that appear to be unique for each species or phase are indicated in bold type. It will be noticed that there are some differences in the assignment of modes between the calculated and the experimental spectra. However, a detailed discussion of peak

TABLE 11: Normal Vibrational Frequencies (cm^{-1}) for Selected Model Clusters, Calcium Orthophosphate Minerals, and Bone[a]

$[Si_3O_6H_5(H_2O)_3]^-$	$[Si_3O_6H_5CaHPO_4(H_2O)_3]^-$	DCPD	OCP	HAP[b]	young enamel and young bone	mature bone
	295 Ca−O bend					
303, 310, 333, 352 $O_{br}SiO_t$bend	303, 315 SiO_t bend; Si−O_{br} bend					
	358, 379 OPO bend, Ca−O stretch?	337, 363 lattice mode	337 Ca−H_2O translations			
	384, 392 Si−O_{br} bend	394 OPO bend				
404, 408, 410 H_2O libration? + $O_{br}SiO_tH$ bend or stretch?	438, 456 H_2O libration?		445 H_2O libration			
	445 OPO bend		465 PO_4 bend ν_2	472		467, 470 PO_4 bend ν_2
448 $O_{br}SiO_t^-$ bend 466, 485 SiO_tH bend + H_2O libration?	481, 491 Si−O_{br} stretch?					
	494, **514** O_{br} breathing					
	577, 584 OPO bend	519, 535, 583 OPO bend	529, 561, 578 PO_4 bend ν_4; HPO_4 bend ν_4	541, 575	560	565, 579 PO_4 bend ν_4
596, **651** O_{br} breathing						
663 SiO_{br} bend	**632**, **636** PO_4 bend + SiO_{br} bend?		599, 608 PO_4 bend ν_4	601, 631 (631 band missing in CO_3−HAP[b])	**610**, **615**	601 PO_4 bend ν_4
	678 (Ca)H_2O libration?	663, 665 H_2O libration	627, 650 H_2O libration			
	681					
	687 H_2O libration?					
	636 Si−O_{br} bend?					
720 $SiO_{br}Si$ stretch	712, 716 Si−O_{br} stretch					
		785 POH bend				
	818, 822 Si−H bend					
853 $O_{br}SiH$ bend?	859 H_2O bend					
877 H_2O bend?	877 SiO_tH stretch					
	886 P−OH symmetric stretch	875 P−OH stretch	873 P−OH stretch			
						(874 CO_3^{2-} bend ν_2)
898, 911, 933 SiO_tH ν_1 stretch	899 O_tSiO_{br} bend + P−OH stretch					
945, 970, 976 $HSiO_3$ bend or stretch?	908 Si−O_tH stretch					
	925, 953 SiO_tH bend					
	936, 967, 978 SiO_tH bend					
		984, 1000 OPO bend	**913** 963, 967 PO_4 stretch ν_1	962	960−970	PO_4 stretch ν_1
1004 HO_tSiH bend	1000 Si−O_tH stretch					
	1024, 1086 SiO_{br} stretch					
1061,1075, 1091 $HSiO_{3r}$ stretch	1047 SiO_{br} stretch + P−O stretch	1057, 1075 P−OH stretch	1023,1038, 1056, 1086, 1093 PO_4 stretch ν_3	1040, 1092	1020, 1100 HPO_4^{2-} in (HPO_4^{2-} in HAP)	1012, 1046, 1056, 1085, 1096 PO_4 stretch ν_3
	1060 P−O stretch					
1117, 1168 SiO_{br} stretch	**1118** OPO bend?	1123, 1140 P−OH stretch	1109, 1118, 1138 HPO_4 stretch ν_3		**1110**, **1125** (PO_4^{3-} in poorly crystalline HAP); **1145** (HPO_4^{2-})	
	1144 OPO bend					
	1162 Si−O_t^- stretch					
1236 Si−O_t^- ν_1 stretch	1210 PO bend?	1200, 1215 POH bend	1207 HPO_4 OH in−plane bend			
	1262 H_2O bend + SiOH bend?					
	1295 P−O stretch?		**1298** HPO_4 OH in−plane bend			
						1420, 1473, 1620 CO_3^{2-} bend ν_3
1768, 1777, 1862 H_2O bend	1772, 1814, 1834 H_2O bend	1650 H_2O ν_2 bend	1629 H_2O ν_2 bend			
				1985		
2257	2369, 2416, 2421 Si−H stretch					
2347						
2358 Si−H stretch						
		2140, 2270, 2380, 2930 ν_1 P−O stretch	2400, 2950 HPO_4 OH stretch	2000, 2050, 2075, 2140		
3670 H_2O stretch	3573, 3867, 3971 H_2O stretch	3160, 3280, 3490, 3545 ν_1, ν_3 H_2O stretch	3555 ν_1, ν_3 stretch of H-bonded H_2O, HPO_4 O−H stretch	3570		
	3591, 3664, 3788 SiO_t−H stretch					
4004, 4010, 4087 H_2O stretch	4104 PO−H ν_1 stretch					
4089 SiO−H ν_1 stretch						
4130 H_2O stretch						

[a] Normal IR and/or Raman vibrational frequencies and assignments for $[Si_3O_6H_5(H_2O)_3]^-$ and $[Si_3O_6H_5CaHPO_4(H_2O)_3]^-$ were calculated at the HF level with the valence double-ζ basis set. Experimentally measured IR vibrational frequencies and assignments were taken from the literature for DCPD, HAP, and OCP,[66−68] young enamel and young bone,[69−70] and mature bone.[71] Vibrational features unique to each species or phase are shown in bold type. [b] Bone-mineral is more similar to dahllite, a carbonated apatite (CO_3−HAP), rather than to pure HAP.

assignments for calcium orthophosphate minerals is beyond the scope of the present paper, so we will mainly concentrate here on comparing the peak positions.

The characteristic Raman-active breathing modes of bridging oxygens O_{br} in planar 3-rings and planar 4-rings occur at 605 and 495 cm^{-1}, respectively.[32] The 3- and 4-rings are defect sites denoted D_2 and D_1. In the model cluster $[Si_3O_6H_5(H_2O)_3]^-$ the breathing modes occur at 596 and 651 cm^{-1}, close to the expected value of 605 cm^{-1}. The hydrogen atom terminations to the silicon cluster and the one deprotonated silanol site result in our model cluster not being perfectly symmetrical. As a result, instead of the single sharp peak at 605 cm^{-1}, we calculate that this peak is split into two peaks at 596 and 651 cm^{-1}. An important result that emerges on comparing the results for cluster $[Si_3O_6H_5(H_2O)_3]^-$ with $[Si_3O_6H_5CaHPO_4(H_2O)_3]^-$ is that oxygen breathing modes have shifted to 494 and 514 cm^{-1}, which are almost identical to the value of 495 cm^{-1} expected for the D_1 defect corresponding to the uncomplexed 4-ring[32] (Table 11).

The combination bands that are predominantly due to motions of the HPO_4^{2-} moiety in the $[Si_3O_6H_5CaHPO_4(H_2O)_3]^-$ cluster are at 358, 379, 445, 577, 584, 632, 636, 886, 899, 1060, 1118, 1144, 1210, 1295, and 4103 cm^{-1}. The assignments are indicated in Table 11. Many of these bands are common to $[Si_3O_6H_5CaHPO_4(H_2O)_3]^-$, DCPD, OCP, HAP, young enamel and bone, and mature bone (Table 11). It appears that the bands at 785 cm^{-1} and at 913 and 1298 cm^{-1} are unique to and hence characteristic of DCPD and OCP, respectively. The spectrum of HAP is unique from the other minerals and from $[Si_3O_6H_5CaHPO_4(H_2O)_3]^-$in the lack of any bands at ~1110, 1120, and 1140 cm^{-1}. In this respect, the spectrum of mature bone is similar to that of HAP, but distinct from those of young bone and enamel, which have features at 1110, 1125, and 1145 cm^{-1}. The spectrum for HAP also lacks bands at ~862−875 cm^{-1}. The spectrum for mature bone does have a peak at 874 cm^{-1}, but bone is a carbonated apatite (dahllite), and this band has been assigned to the CO_3^{2-} ν_2 bending mode.[71] If this assignment is correct, then mature and young bone, similar to HAP, lack a PO_4 mode at 874 cm^{-1}. Finally, young bone and enamel are also distinct from mature bone in having a peak at 610−615 cm^{-1}. This feature also distinguishes young bone from all the minerals except HAP, which has a peak at 631 cm^{-1}. However, the spectrum for a carbonated apatite which may be considered as a more appropriate model than HAP for bone mineral (dahllite) lacked the 631 cm^{-1} band.[70] The calculated spectrum for the $[Si_3O_6H_5CaHPO_4(H_2O)_3]^-$ cluster has peaks at 632 and 636 cm^{-1}, similar to those of young bone and enamel.

The calculated spectrum of model clusters $[Si_3O_6H_5(H_2O)_3]^-$ and $[Si_3O_6H_5CaHPO_4(H_2O)_3]^-$, young bone, and mature bone can also be compared to the IR spectrum for silica gels reacted with simulated body fluids for different lengths of time[15,72] (Figure 6). The unreacted silica gels would correspond to $[Si_3O_6H_5(H_2O)_3]^-$ (strictly speaking, $[Si_3O_6H_6(H_2O)_3]^0$), the reacted gels at 4 and 6 days would correspond to intermediate stages such as $[Si_3O_6H_5CaHPO_4(H_2O)_3]^-$, and the reacted gels at 30 days would correspond to mature bone.

Before reaction the glass has a very broad band from ~1000 to 1150 cm^{-1}, and only slightly narrower bands at ~800 and ~450 cm^{-1}. These bands are comparable to the calculated frequencies for the unreacted model cluster $[Si_3O_6H_5(H_2O)_3]^-$ (Table 11 and Figure 6). After reaction of the silica gel glass with SBFs for 4 days, the broad band at ~1150−1000 cm^{-1} widens slightly up to ~1200 cm^{-1}. This peak may be identified with the 1210 cm^{-1} peak predicted for $[Si_3O_6H_5CaHPO_4(H_2O)_3]^-$.

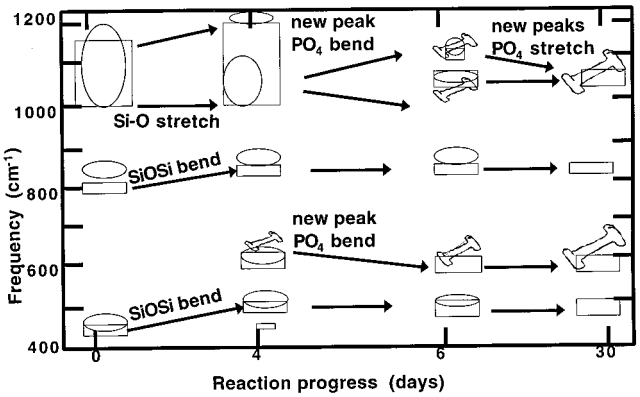

Figure 6. Schematic representation of changes in vibrational modes during reaction progress for (a) bioceramic reacting with simulated body fluid (rectangles), (b) model clusters $[Si_3O_6H_5(H_2O)_3]^-$ and $[Si_3O_6H_5CaHPO_4(H_2O)_3]^-$ (ovals), and (c) earliest mineral deposits in young bone to mature bone (cartoon bone). The size of cartoon bone increases as bone matures. Note that the *x* axis is not scaled.

After 6 days, this broad band splits up, and after one month of reaction the band has moved to about 1050 cm^{-1} with a small shoulder remaining at ~1100 cm^{-1}. The 1050 cm^{-1} band was assigned by the original authors[15] to the P−O stretch in HAP. It is also close to the 1056 band seen in mature bone. At 6 days, the ~1100 cm^{-1} band seen in the reacting gel may be associated with the 1110 band in young bone, and at 30 days with the 1096 cm^{-1} band in mature bone (Table 11 and Figure 6). These bands seen for the reacting gel are similar to the peaks predicted for $[Si_3O_6H_5CaHPO_4(H_2O)_3]^-$ at 1060 and 1118 cm^{-1}.

The bands at ~800 and ~450 cm^{-1} for the gel are characteristic of Si−O bending modes and are evident after 4 days of reaction. But after 6 days, the band at 800 cm^{-1} has shifted to ~850 cm^{-1}, and the 450 cm^{-1} band is diminished (Figure 6). By 30 days, the 450 cm^{-1} band is no longer present. Comparable shifts are seen on going from $[Si_3O_6H_5(H_2O)_3]^-$ to $[Si_3O_6H_5CaHPO_4(H_2O)_3]^-$, where the 853 cm^{-1} bending mode moves to 877 cm^{-1}, and the 448−466 cm^{-1} band associated with SiO bending disappears. New bands are seen emerging after 4 days of gel reacting with SBFs at ~550−600 cm^{-1}. In fact, the 600 cm^{-1} peak is quite broad at 4 days and can be considered to be at a position of ~615−600 cm^{-1}. However, the width of the peak precludes the identification of a more precise peak position from the published spectrum.[15] This peak may correspond to the 636 cm^{-1} peak predicted for $[Si_3O_6H_5CaHPO_4(H_2O)_3]^-$ and the 620 cm^{-1} peak observed in young bone. After 6−30 days of reaction, the gel peaks become narrower and the ~>600 cm^{-1} peak moves toward ~590−600 cm^{-1}. These peaks were considered to be characteristic of the P−O bend in crystalline HAP.[15] The shift from ~ 615−600 to ~ 590−600 cm^{-1} corresponds to the change from 615 to 601 cm^{-1} observed on going from young bone to mature bone.

In summary, the Si 3-ring model clusters, reacting bioceramic at 4−6 days, and young bone share common, unique vibrational features at ~615 cm^{-1} and at ~1100, 1110, and 1120 cm^{-1}, which are different from the features seen in mature bone and crystalline apatite.

4. Discussion

4.1. Reaction Pathway for Apatite Precipitation on Bioceramics. Hayakawa et al.[20] immersed a bioceramic in simulated body fluid and obtained a broad ^{29}Si peak that shifted slightly over time. They deconvoluted the broad peak into Q^2, Q^3, and Q^4 types of sites, and obtained a small deshielding of 2−8 ppm

after reaction of bioceramic with SBFs for ~10 min, followed by a small increased shielding of ~0.4−7 ppm after reaction for about 8−12 h. Q^n represents a SiO_4 tetrahedra, with "*n*" of its oxygen atoms bonded to other SiO_4 tetrahedra. These experimental trends were taken as indication of the conversion of Q^2 silica surface groups to Q^3 and Q^4 groups, formation of Si−O−P bonds, and, eventually, breaking of the Si−O−P bonds.

The trends and magnitudes of the average ^{29}Si shielding changes predicted for most of the scheme 2 reaction pathways are consistent with experimental observation, but the overall reaction energies suggest that the reactions are unfavorable (endothermic) or thermoneutral (no change in enthalpy within error) (Tables 8 and 9). The only scheme 2 pathway which is clearly exothermic does have a ^{29}Si shielding trend consistent with experiment. By comparison, the overall reaction energies for scheme 1 pathways are much more exothermic and, hence, more favorable. Several previous studies have used Raman, NMR, and X-ray absorption near edge structure spectroscopy to investigate the issue of direct Si−O−P bond formation in gels and glasses. We are aware of only two experimental studies where direct Si−O−P bonds were reported in low-temperature silicophosphate gels.[73,74] Partial subsititution of P into SiO_4 tetrahedra has been reported only in glasses quenched at high temperatures and with high P contents (>10 mol %).[75] But these high-temperature systems do not correspond to the formation of apatite in simulated body fluids at room temperature. Most studies of alkaline-earth silicophosphate glasses, silicophosphate xerogels, and $SiO_2-CaO-P_2O_5$ bioceramics have shown that Si−O−P bonds do not exist at phosphorus contents of <5 mol %, where Si is in 4-fold coordination.[76−81] A recent ab initio study supports the formation of strong hydrogen-bonded complexes between the phosphate group and the hydroxyl (silanols) on the silica surface, but no results were reported for direct Si−O−P bonds.[82] Finally, the ^{31}P NMR isotropic and anisotropic shifts for several scheme 1 clusters, which were predicted using both 3-21G* and 6-31G* basis sets, resemble values for young bone and orthophosphate minerals. In fact, the isotropic and especially the anisotropic shifts for $[Si_3O_6H_5CaHPO_4(H_2O)_3]^-$ are very similar to the values for brushite. These results are in excellent agreement with the proposal that HPO_4^{2-} ions exist in a brushite-like configuration on the surface of the earliest mineral deposits in embryonic bones.[63] The values for scheme 2 clusters are quite different, and even at the higher basis set the anisotropic shift for $[Si_3O_6H_5PO_3Ca(H_2O)_6]^0$ is not similar to that of young bone. Thus, the combined evidence of our calculated reaction energies, ^{29}Si NMR trends, and ^{31}P shifts along with the results of these previous studies leads us to suggest that scheme 1 is preferred over scheme 2 as the pathway for apatite nucleation.

Calculated trends in ^{29}Si NMR shielding changes for scheme 1 suggest that only pathways involving inner-sphere calcium complexes on the 3-ring are consistent with experiment (Table 9), and the overall reactions are predicted to be exothermic (Table 8). Thus, $[Si_3O_6H_5Ca(H_2O)_6]^+ \rightarrow [Si_3O_6H_5CaHPO_4(H_2O)_3]^-$ or $[Si_3O_6H_5CaH_2PO_4(H_2O)_3]^0$ is the only pathway that satisfies both energy and ^{29}Si shielding criteria relative to the experimental trends. Therefore, we suggest that this is the most favored pathway, although at pH ≈7.3, the pathway $[Si_3O_6H_6Ca(H_2O)_6]^{2+} \rightarrow [Si_3O_6H_6CaHPO_4(H_2O)_3]^0$ cannot be ruled out. In either case, the predicted deshielding of ~19 ppm is much larger than the decrease of about 2−8 ppm observed. One possible explanation for this discrepancy is that the experiment measures an average of all the reactive and unreactive sites present at the surface. We can further narrow the list of most likely clusters by considering the overall energy results in Table 8, which suggests that $[Si_3O_6H_5CaHPO_4(H_2O)_3]^-$ is favored over $[Si_3O_6H_5CaH_2PO_4(H_2O)_3]^0$ and $[Si_3O_6H_3CaH_2PO_4(H_2O)_3]^{2-}$.

4.2. Alkaline-Earth Metal Adsorption. The point of zero charge (pH_{PZC}) for silica is at pH ≈ 3−4,[83] which means that above this pH the silica surface has a net negative charge. The magnitude of the negative charge increases with pH. The magnitude of the charge is small, however, compared to the charge developed on other oxide surfaces at an equivalent number of pH units above their pH_{PZC}. In a separate study, we have calculated the deprotonation pK_a for the Si 3-ring to be about 6.0.[84] Thus, in the near-neutral pH range of interest to our study, the silica surface is dominated (>90%) by neutral sites represented in our model as $[Si_3O_6H_6]^0$ with a small number of negatively charged sites represented here as $[Si_3O_6H_5]^-$. Much effort as been spent in determining whether alkaline-earth cations such as Ca^{2+}, Sr^{2+}, and Ba^{2+} sorb as inner-sphere or outer-sphere complexes (refs 85−88 and references therein). Our calculations predict that the nature of the complex changes with pH. The lighter alkaline-earth ions, Mg^{2+} and Ca^{2+}, adsorb as outer-sphere surface complexes at the fully protonated, neutral surface sites (N. Sahai, unpublished results for Mg^{2+}). That is, no direct bonds are made between the cation and O_tH, which implies that these ions prefer to bond to the O_w of solvating water molecules rather than to the surface oxygen (O_tH) atoms. When the surface has a small negative charge (O_t^-), the inner-sphere species is energetically preferred over the outer-sphere complex and the surface hydroxide. Finally, at very high pH when the surface has a large negative charge represented here as $[Si_3O_6H_3]^{3-}$, the surface hydroxide becomes more stable than the inner-sphere complex.

4.3. pH Effects. As discussed above, with increasing pH, we find that the ability of various oxygen ligands to compete for alkaline-earth metal ions increases as: solvating water < negatively charged surface silanol < hydroxide. Thus, the negatively charged surface is capable of promoting partial cation dehydration with formation of the inner-sphere complex. A caveat in applying these results to equilibrium adsorption models is that the Si 3-ring is a reactive, defect site and not necessarily representative of the average silica surface.

The charge on the surface clusters depends on both the protonation level of the Si ring and the protonation level of the phosphate ion. Table 8 indicates that the complexes involving HPO_4^{2-} are more stable than those with $H_2PO_4^-$ or PO_4^{3-}. The greater stability of the acidic HPO_4^{2-} ion relative to PO_4^{3-} intermediates is in accordance with Ostwald's rule of stages. According to this rule, the more soluble phase (DCPD) nucleates as a precursor to the less soluble phases (OCP and HAP), thus providing the surface energy needed for subsequent apatite growth.[89]

4.4. Representation of the Silica Bioceramic Surface and the Nucleating Cluster. In the preceding discussion we have assumed that the silicon 3-ring is the appropriate model for the nucleating site on the bioceramic surface, as did West and Hench.[22] In fact, 3-rings have been identified by Raman spectroscopy as defect sites in silica glasses and sol−gels by their characteristic oxygen breathing mode at 605 cm^{-1}.[32−34] In contact with pure water 3-rings become destabilized due to strain energy associated with the ring structure,[23,27] and are hydrolyzed within about 24 h.[34] In the case of bioceramics, the characteristic Raman-active band at 605 cm^{-1} associated with 3-rings disappeared after reaction with SBFs for 1 day,[18] whereas the characteristic peak for 4-rings at 495 cm^{-1} appeared

unchanged. These results were taken to indicate that 3-rings are dissolved away and are not necessary for apatite nucleation.[18] Although this interpretation may be correct, their results can be interpreted in other ways. For instance, it is possible that in the 3-rings promote the formation of the precursor surface complex before being hydrolyzed. So, even if the ring is not preserved beyond the first day of immersion in SBFs, the critical nucleus has already formed, which provides the surface energy required for subsequent growth. Formation of the surface complex may shift the characteristic 605 cm^{-1} Raman peak to some other part of the spectrum such as to the 495−500 cm^{-1} region as predicted by our calculations (Table 11). Alternatively, it is possible that in aqueous solutions containing ions the 3-rings are not as unstable as in pure water. Thus, the lack of the D_2 characteristic band at 605 cm^{-1} in SBF-*reacted* bioceramics does not necessarily imply the absence of 3-rings, nor does the presence of the 495 cm^{-1} band in the SBF-*reacted* bioceramic necessarily imply the presence of 4-rings. Similarly, if the characteristic oxygen breathing mode of the 4-ring at 495 cm^{-1} had shifted due to surface-complex formation, it would not necessarily be evident from the Raman spectrum, as the 495 cm^{-1} band due to the oxygen breathing mode of the cluster $[Si_3O_6H_5CaHPO_4(H_2O)_3]^-$ would still be observed at the same frequency. Thus, the presence of the 495 cm^{-1} band does not necessarily imply that the 4-rings have not reacted. This discussion shows that Raman spectra alone cannot be used as a diagnostic tool to determine the reactivity of Si 3- and 4-rings in apatite nucleation. Indeed, our calculations indicate that the 3-ring promotes formation of an acidic surface complex with spectral features similar to those of reacting bioceramics and to the earliest mineral deposits in bone. The geometry and spectral features for the surface complex on the 4-ring are quite different. The 4-rings and the double rings with open cube structure ($[Si_7O_{12}H_{10}]$) are relatively more stable than 3-rings, which makes them unlikely candidates for the active site. Therefore, one way of interpreting our results is to consider the large $[Si_7O_{12}H_{10}]$ ring clusters as representative of the average surface site, and the 3-rings as the active defect sites of higher energy. There is also a practical bonus as the open double ring requires much greater computational effort compared to the 3-rings especially when $CaHPO_4$ and water molecules are included. We conclude, then, that the 3-ring is the reactive site on the silica bioceramic surface. The partially deprotonated ring promotes nucleation of the acidic precursor surface complex before the ring is hydrolyzed.

The 3-rings modeled here directly represent the actual active site. The $CaHPO_4(H_2O)_3$ cluster sorbed onto the $[Si_3O_6H_5]^-$ ring, however, is a model cluster representing a portion of the actual nucleating cluster that initiates precipitation. This brings us to the issue of the size of the nucleating cluster. In our model cluster, $[Si_3O_6H_5CaHPO_4(H_2O)_3]^-$, the size of the calcium hydrogen phosphate unit is about 4−4.5 Å. Intensity-enhanced light-scattering experiments have shown the presence of stable calcium phosphate clusters in solutions supersaturated with respect to apatite.[91] These clusters were about 0.7−1.0 nm in diameter, which is much smaller than the size expected from traditional nucleation theory. However, clusters of subcritical size are predicted from nucleation theory if the size dependence of surface tension is taken into account.[92,93] Using the Onuma and Ito[91] study as a guide, the size of our model $CaHPO_4$ cluster suggests that the actual nucleating cluster on the silica surface is only about 2 or 3 $CaHPO_4$ units large, and may be represented by a formula such as $[Si_3O_6H_5(CaHPO_4(H_2O)_3)_n]^-$, $n = 2$ or 3. We call this cluster the acidic, precursor complex or acidic, precursor oligomer or nucleating cluster. With this small size of the nucleating cluster, our model approximation of using only one $CaHPO_4$ cluster should be sufficient to capture the essential energetics and spectral properties. This can be compared to model clusters such as $Si_2O_7H_6$ which are used quite successfully for modeling entire silica surfaces.[25,26]

4.5. Effect of the Surface on Nucleation. As summarized in ref 91, different processes have been proposed as the limiting step in homogeneous nucleation of HAP such as dehydration and diffusion of the calcium ion, and addition of hydroxide ions.[94−97] Our study shows that the negatively charged Si 3-ring on the bioceramic surface promotes the dehydration of the calcium. This prediction is supported by experiments which showed that surfaces with a negative electric potential accelerated nucleation and growth of HAP compared to positively charged surfaces.[98] By driving the adsorption reaction, the presence of the surface promotes the formation of the precursor oligomer nuclei. Although the calculations in this study do not directly address the subsequent step which leads from the nucleating cluster to the surface precipitate, we can envision the process on the basis of reported literature. Although this part of the paper is speculative, we believe that it is important to lay out this proposed sequence of events to explain published experimental observations in terms of our calculations.

3-Rings are present on silica gels prepared from different starting solutions, but only silica gels prepared in PEG-containing solutions are able to promote apatite precipitation.[18,19] This does not necessarily mean that some dissolved silicate species is involved in nucleation. Kokubo, Cho, and coworkers[18,19] suggested that a special structure associated with silica gels synthesized in PEG-containing solutions may be necessary to promote apatite nucleation, although they were unable to identify this special structure by Raman spectroscopy. We suggest an alternative explanation for their experimental obervations while simultaneously satisfying our proposal that negatively charged 3-rings nucleate critical clusters such as $[Si_3O_6H_5(CaHPO_4(H_2O)_3)_n]^-$, $n = 2$ or 3. The 3-rings may be hydrolyzed soon after these acidic surface oligomers form, although this step is not crucial to the argument. We propose that aggregation of the oligomers is a necessary step for the growth of crystallites and their subsequent solid-state transformation into apatite crystals large enough to be detected by X-ray diffraction. This last step is in accord with recent reports of solid-state transformation in biomimetic synthesis of silica-based micellar structures, calcite, and barium titanate.[99] It is at the aggregation step that the role of PEG is proposed to be important. PEG is a polymer that may be represented as $HO-CH_2CH_2\cdots CH_2-O-CH_2\cdots CH_2CH_2-OH$. We propose that the hydroxyl terminations on PEG are responsible for assisting in the aggregation of the calcium orthophosphate oligomers, perhaps by H-bonding with the HPO_4 moiety on the calcium orthophosphate oligomers. Polynuclear mechanisms have also been proposed in some recent studies of homogeneous HAP precipitation.[97,100] The suggested role of OH terminations in assisting oligomer aggregration goes beyond the calculations in the present study, but is consistent with some other interesting experimental obervations. Silica phytoliths isolated from bamboo are found to be capable of promoting apatite precipitation.[17] Soluble polymers associated with silica phytoliths are carbohydrate-rich with many hydroxyl groups.[101] In a separate study on the precipitation of silica, it was found that cellulose, a carbohydrate, does not promote the actual silica nucleation rate but does promote aggregation of silica oligomers.[102]

TABLE A1: Table of Bond Lengths for Selected Clusters with Geometries Optimized at the Self-Consistent Level Using Effective Core Potentials and Valence Double-ζ Basis Sets

bond	bond length (Å)	bond	bond length (Å)
		$[Si_3O_6H_6(H_2O)_3]^0$	
$Si-O_{br}$	1.64	$O_t(H)-O_w$	2.96
$Si-O_{tH}$	1.62	$Si-H$	1.48
		$[Si_3O_6H_5(H_2O)_3]^-$	
$Si-O_{br}$	1.63, 1.64	$O_t^-—H_w$	1.71
$Si-O_t^-$, $Si-O_tH$	1.62, 1.62	$Si-H$	1.49
$O_t(H)-O_w$	3.05		
		$[Si_3O_6H_3(H_2O)_3]^{3-}$	
$Si-O_{br}$	1.66	$O_t^-—H_w$	1.63
$Si-O_t^-$	1.57	$Si-H$	1.53
		$[Si_3O_6H_6(H_2O)_3Ca(H_2O)_3]^{2+}$	
$Si-O_{br}$	1.64	$SiO_t(H)-Ca$	2.30, 2.36, 2.34, 2.43, 2.47, 2.49
$Si-O_tH$	1.63	$Si-Ca$	5.55, 5.57, 5.68
$SiO_t(H)-O_w$	4.47		
		$[Si_3O_6H_6Ca(H_2O)_6]^{2+}$	
$Si-O_{br}$	1.63	$\langle Ca-O_{w1}\rangle$	2.30
$Si-O_tH$	1.69	$\langle Ca-O_{w1}\rangle$ ($\langle Ca-O_{w2}\rangle$)	4.53, 4.52, 4.62 $\langle 4.53\rangle$
O_tH-Ca	2.42	$Si-Ca$	3.63, 3.64, 3.69
		$[Si_3O_6H_5Ca(H_2O)_6]^+$	
$(O_t^-Si)-O_{br}$	1.69	$Ca-O_{w1}$ ($\langle Ca-Ow_1\rangle$)	2.29, 2.31, 2.32 (2.31)
$(HO_tSi)-O_{br}^-$	1.60, 1.64	$Ca-O_{w2}$ ($\langle Ca-O_{w2}\rangle$)	4.61, 4.67, 4.69 (4.66)
$Si-O_t^-$	1.57	$(O_t^-)Si-Ca$	3.32
$Si-O_tH$	1.69	$(O_tH)Si-Ca$	3.65, 3.54
$O_t^-—Ca$	2.09		
		$[Si_3O_6H_3Ca(H_2O)_6]^-$	
$Si-O_{br}$	1.66	$Ca-O_{w1}$ ($\langle Ca-O_{w1}\rangle$)	2.36
$Si-O_t^-$	1.59	$Ca-O_{w2}$ ($\langle Ca-O_{w2}\rangle$)	4.91
$O_t^-—Ca$	2.21	$Si-Ca$	3.22
		$[Si_3O_6H_6(OH)_3Ca(H_2O)_3]^-$	
$Si-O_{br}$	1.64	$O_wH^-—Ca$	2.21
$Si-O_tH$	1.61	$Ca-O_w$	2.46
$SiO_t(H)-O_wH^-$	2.69	$Si-Ca$	4.65
$SiO_t(H)-Ca$	4.11		
		$[Si_3O_6H_6CaHPO_4(H_2O)_3]^0$	
$Si-Ca$	3.64	$Ca-P$	2.80
$Ca-O_{tH}$	2.42	$P-O_{1P}$, $P-O_2P$	1.54
$Ca-O_w$	2.41, 3.87, 3.94	$P-O_PH$	1.61
$Ca-O_{1P}$	2.22	$P=O$	1.49
$Ca-O_{2P}$	2.14		
		$[Si_3O_6H_5CaHPO_4(H_2O)_3]^-$	
$Si-Ca$	3.31, 3.54, 3.62	$Ca-P$	2.77
$Ca-O_tH$, $Ca-O_t^-$	2.43, 2.12	$P-O_1P$, $P-O_2P$	1.55, 1.53
$Ca-O_w$	3.57, 3.76, 4.0	$P-O_PH$	1.61
$Ca-O_{1P}$	2.22	$P=O$	1.49
$Ca-O_{2P}$	2.17		
		$[Si_3O_6H_3CaHPO_4(H_2O)_3]^{3-}$	
$Si-Ca$	3.22	$Ca-P$	3.39
$Ca-O_t^-$	2.22	$P-O_1P$	1.54
$Ca-O_w$	3.74, 4.11, 4.14	$P-O_PH$	1.67
$Ca-O_{1P}$	2.11	$P-O_{2P}^-$ $P=O$	1.51, 1.51

A careful consideration of the ^{29}Si NMR, IR, Raman, and XRD data for bioceramic reacting with simulated body fluids[18,20,72] provides us with an estimate for the rate of the reaction. The adsorption of calcium and phosphate ions resulting in nucleation of the oligomer is the fastest step, occurring within minutes to ~1 h, resulting in the initial decrease and then increase in ^{29}Si NMR shieldings. The hydrolysis of the Si 3-ring, if it occurs, takes place within the first day (~24 h) of reaction with SBFs. Finally, the aggregation of oligomers and transformation to apatite crystals sufficiently large to be detected by X-ray diffraction is the slowest step, taking about 2 weeks.

5. Conclusions

A combined approach using predicted geometries, energies, NMR shieldings, and normal vibrational modes shows that at the near-neutral pH range of blood plasma the planar Si 3-ring is the active surface site on silica biocermics. Ca^{2+} sorbs as an inner-sphere complex at the negatively charged surface site followed by HPO_4^{2-}, resulting in an acidic, hydrated, precursor cluster with 2−3 units of calcium hydrogen phosphate. The predicted precursor is a surface complex or surface oligomer, not a well-defined mineral phase. This may explain the past difficulty in identifying the precursor by traditional spectroscopic or microscopic methods. The predicted precursor, reacting bioceramic, and early mineral deposits in bone share common ^{29}Si and ^{31}P NMR shifts and IR/Raman vibrational peaks which are distinct from those observed in mature bone and crystalline apatite. After the initial nucleation of the acidic precursor surface oligomer, we speculate that the mechanism involves aggregation and growth of oligomers by H-bonds with subsequent transformation to crystalline apatite.

Acknowledgments. N.S. thanks Prof. Alan T. Stone of the Department of Geography and Environmental Engineering, Johns Hopkins University, Baltimore, for helpful discussions and for identifying bibliography that was instrumental in the development of this work. This study was supported by an NSF Earth-Sciences Postdoctoral Fellowship No. EAR 9805673 to N.S. and by DOE Grant No. DE- FG02- 94 ER144467 to J.A.T.

Appendix

Table A1 lists bond lengths for selected clusters.

References and Notes

(1) Lowenstam, H. A.; Weiner S. *On Biomineralization*; Oxford University Press: Oxford, 1988; Chapter 9, pp 144−188.
(2) Elliot, J. C. *Structure and Chemistry of the Apatites and Other Calcium Orthophosphates*; Elsevier: Amsterdam, 1994.
(3) Boskey, A. L. *J. Cell. Biochem. Suppl.* **1998**, *30/31*, 83.
(4) Glimcher, M. J. *Metabolic Bone Disease and Clinically Related Disorder*, 3rd ed.; Academic Press: New York, 1998; p 23.
(5) Hench, L. L. In *Bioceramics*; Duchyne, P., Lemons, J., Eds. *Ann. N.Y. Acad. Sci*. **1988**, *523*, 54.
(6) Gross, U.; Kinne, R.; Schmitz, H. J.; Strunz, V. *CRC Crit. Rev. Biocompatibility* **1988**, *4*, 2.
(7) Kokubo, T. *J. Non-Cryst. Solids* **1990**, *120*, 138.
(8) Rehman, I.; Hench, L. L.; Bonfield, W. In *Bioceramics 6*; Ducheyne, P., Christiansen, D., Eds.; Butterworth-Heinemann Ltd.: London, **1993**; p 123.
(9) Galliano, P. G.; Porto Lopez, J. M. *Anais do II Congresso Iberoamericano de Ceramica, Vidro e Refractario* **1991**, *758*.
(10) Hench, L. L. *Bioceramics* **1990**, *3*, 43.
(11) Kokubo, T. *Biomaterials* **1991**, *12*, 155.
(12) Li, P.; Ohtsuki, C.; Kokubo T.; Nakanishi, K.; Soga, N.; Nakamura, T.; Yamamuro, T. *J. Mater. Sci.: Mater. Med*. **1993**, *4*, 127.
(13) Andersson, O. H. *Bioceramics* **1995**, *8*, 483.
(14) Cho, S. B.; Miyaji, F.; Kokubo, T.; Nakanishi, K.; Soga N.; Nakamura, T. *Bioceramics* **1995**, *8*, 493.
(15) Pereira, M.; Hench, L. L. *J. Sol-Gel Sci. Technol.* **1996**, *7*, 59.
(16) Kokubo, T.; Ito, S.; Huang, Z. T.; Hayashi, T.; Sakka, S.; Kitsugi, T.; Yamamuro, T. *J. Biomed. Mater. Res.* **1990**, *24*, 331.
(17) Li, S. H.; Liu, Q.; de Wijn, J.; Zhou, B. L.; de Groot, K. *J. Mater. Sci.: Mater. Med.* **1997**, *8*, 427.
(18) Cho, S. B.; Nakanishi, K.; Kokubo, T.; Soga, N.; Ohtsuki, C.; Nakamura, T. *J. Biomed. Mater. Res. (Appl. Biomater.)* **1996**, *33*, 145.
(19) Cho, S. B.; Miyaji, F.; Kokubo, T.; Nakanishi, K.; Soga, N.; Nakamura, T. *J. Mater. Sci.: Mater. Med.* **1998**, *9*, 279.
(20) Hayakawa, S.; Iida, S. T.; Ohtsuki, C.; Osaka, A. *Phys. Chem. Glasses* **1996**, *37*, 188.
(21) Kasemo, B.; Lausmaa, J. In *Surface Characterization of Biomaterials*; Ratner, B. D., Ed.; Elsevier: Amsterdam, 1988; p 1.
(22) West, J. H.; Hench, L. L. In *Bioceramics 5*; Yamamuro, T., Kokubo, T., Nakamura, T., Eds.; Kobunshi Kankokai: Kyoto, 1991; p 75.
(23) West, J. K.; Wallace, S. *J. Non-Cryst. Solids* **1993**, *152*, 109.
(24) Dahlin, S.; Ångstrom, J.; Linde, A. *Eur. J. Oral Sci*. **1988**, *106*, 239.
(25) Gibbs, G. V. *Am. Mineral*. **1982**, *67*, 521.
(26) Sauer, J. *Chem. Rev.* **1989**, *89*, 199.
(27) Wallace, S.; West, J. K.; Hench, L. L. *J. Non-Cryst. Solids* **1993**, *152*, 101.
(28) Hammond, G. S. *J. Am. Chem. Soc*. **1955**, *77*, 334.
(29) Taube, H. *J. Chem. Educ.* **1959**, *36*, 451.
(30) Schmidt, M. W.; et al. *J. Comput. Chem.* **1993**, *154*, 1347.
(31) Stevens, W. J.; Krauss, M.; Basch, H.; Jansen, P. G. *Can. J. Chem*. **1992**, *70*, 612.
(32) Galeener, F. L. *Solid State Commun*. **1982**, *44*, 1037.
(33) Brinker, C. J.; Tallant, D. R.; Roth, E. P; Ashley, C. S. *J. Non-Cryst. Solids* **1986**, *82*, 17.
(34) Brinker, C. J.; Kirkpatrick, R. J.; Tallant, D. R.; Bunker, B. C.; Montez, B. *J. Non-Cryst. Solids* **1988**, *99*, 418.
(35) Feher, F. J.; Newman, D. A.; Walzer, J. F. *J. Am. Chem. Soc.* **1989**, *111*, 1741.
(36) Tossell, J. A. *J. Phys. Chem*. **1996**, *100*, 12828.
(37) Rashin, A. A.; Honig, B. *J. Phys. Chem.* **1985**, *89*, 5588.
(38) Frisch, M. J.; et al. *Gaussian 94*, Rev. B.3; Gaussian Inc.; Pittsburgh, 1995.
(39) Claverle, P.; Dudley, J. P.; Langlet, J.; Pullman, B.; Piazzola, D.; Huron, M. J. *J. Phys. Chem*. **1978**, *82*, 405.
(40) Freitas, L. C. G.; Longo, R. L.; Simas, A. M. *J. Chem. Soc., Faraday Trans*. **1992**, *88*, 189.
(41) Parchment, O. G.; Vincent, M. A.; Hillier, I. H. *J. Phys. Chem*. **1996**, *100*, 9689.
(42) Tossell, J. A. T. *Am. Mineral*. **1999**, *84*, 877.
(43) Furberg, S. *Acta Chem. Scand.* **1955**, *9*, 1157.
(44) Mighell, A. D.; Smith, J. P.; Brown, W. E. *Acta Crystallogr*. **1969**, *B 25*, 776.
(45) Chapman, A. C.; Thirlwell, L. E. *Spectrochim. Acta* **1964**, *20*, 937.
(46) Schulze, H.; Weinstock, N.; Muller, A.; Vandrist, G. *Spectrochim. Acta* **1973**, *29A*, 1705.
(47) Hehre, W. J.; et al. *Ab Initio Molecular Orbital Theory*; Wiley: New York, 1986.
(48) Wolinski, K.; Hinton, J. F.; Pulay, P. *J. Am. Chem. Soc*. **1992**, *112*, 8251.
(49) Frisch, M. J.; et al. *Gaussian 98*, Revision A.7, Windows version; Gaussian Inc.: Pittsburgh, 1998.
(50) Harris, R. K.; Knight, C. T. G. *J. Chem. Soc., Faraday Trans.* **1983**, 1525, footnote to Table 2.
(51) Kennedy, J. D.; McFarlane, W. In *Multinuclear NMR*; Mason, J., Ed.; Plenum Press: New York, 1987; Chapter 11, p 314.
(52) Wijnen, P. W. J. G.; Beelen, T. P. M.; De Haan, J. W.; Van De Ven, L. J. M.; Van Santen R. A. *Colloids Surf.* **1990**, *45*, 255.
(53) Jones, R. A. Y.; Katritzky A. R. *J. Inorg. Nucl. Chem*. **1960**, *15*, 193.
(54) Crutchfield, M. M.; Callis, C. F.; Irani, R. R.; Roth, G. C. *Inorg. Chem*., **1962**, *4*, 813.
(55) Rothwell, W. P.; Waugh, J. S.; Yesinowski, J. P. *J. Am. Chem. Soc.* **1980**, *102*, 2637.
(56) Sauer, J.; Ahlrichs, R. *J. Chem. Phys.* **1990**, *93*, 2575.
(57) Fleischer, U.; Kutzelnigg, W.; Bleiber, A.; Sauer, J. *J. Am. Chem. Soc.* **1993**, *115*, 7833.
(58) Keith, T. A.; Frisch, M. J. In *Modeling the Hydrogen Bond*; Smith, D. A., Ed.; ACS Symposium Series 569; American Chemical Society: Washington, DC, 1994; Chapter 3.
(59) Ben Naim, A.; Marcus, Y. *J. Chem. Phys*. **1984**, *81*, 2016.
(60) Tawa, G. J.; Topol, I. A.; Burt, S. K.; Caldwell, R. A.; Rashin, A. A. *J. Chem. Phys.* **1998**, *109*, 4852.
(61) Bode, B. M.; Gordon, M. S. *J. Mol. Graphics Mod.* **1998**,*16*, 133.
(62) Miquel, J. L.; Facchini, L.; Legrand, A. P.; Marchandise, X.; Lecouffe, P.; Chanavaz, M.; Donazzan, M.; Rey, C.; Lemaitre, J. *Clin. Mater*. **1990**, *5*, 115.
(63) Roberts, J. E.; Bonar, L. C.; Griffin; Glimcher, M. J. *Calcif. Tissue Int.* **1992**, *50*, 42.
(64) Wu, Y.; Glimcher, M. J.; Rey, C.; Ackerman, J. L. *J. Mol. Biol*. **1994**, *244*, 423.
(65) Aramini, J. M.; Drakenberg, T.; Hiraoki, T.; Yue, K.; Katsutoshi, N.; Vogel, H. J. *Biochemistry* **1992**, *31*, 6761.
(66) Casciani, F.; Condrate, R. A., Sr. *Spectrosc. Lett.* **1979**, *12*, 699.
(67) Fowler, B. O.; Moreno, E. C.; Brown, W. E. *Arch. Oral Biol.* **1966**, *11*, 477.
(68) Fowler, B. O.; Markovic, M.; Brown, W. E. *Chem. Mater*. **1993**, *5*, 1417.
(69) Rey, C.; Shimizu, M.; Collins, B.; Glimcher, M. J. *Calcif. Tissue Int.* **1991**, *46*, 384.
(70) Rey, C.; Shimizu, M.; Collins, B.; Glimcher, M. J. *Calcif. Tissue Int.* **1991**, *49*, 383−388.
(71) Rehman, I.; Bonfield, W. In *Bioceramics 8*; Hench, L. L., Greenspan, D., Eds.; Elsevier Science Ltd.: New York, **1995**, 163.
(72) Pereira, M. M.; Clark, A. E.; Hench, L. L. *J. Am. Ceram. Soc.* **1995**, *78*, 2463.
(73) Jabra, R.; Phalippou, J.; Prassas, M.; Zarzycki, J. *J. Chim. Phys. Phys.-Chim. Biol.* **1981**, *78*, 777.
(74) Tian, F.; Pan, L.; Wu, X. *J. Non-Cryst. Solids* **1988**, *104*, 129.
(75) Fleet, M. E.; Muthupari, S.; Kasrai, M.; Prabakar, S. *J. Non-Cryst. Solids* **1997**, *220*, 85.
(76) Nelson, C.; Tallant, D. R. *Phys. Chem. Glasses* **1984**, *25*, 31.
(77) Yang, W.-H.; Kirkpatrick, R. J. *Commun. Am. Ceram. Soc.* **1986**, *69*, C-222.
(78) Szu, S.-P.; Klein, L. C.; Greenblatt, M. *J. Non-Cryst. Solids* **1992**, *143*, 21.
(79) Livage, J.; Barboux, P.; Vandenborre, M. T.; Schmutz, C.; Taulelle, F. *J. Non-Cryst. Solids* **1992**, *147/148*, 18.
(80) Galliano, P. G.; Porto-Lopez, J. M.; Varetti, E. L.; Sobrados, I.; Sanz, J. *Mater. Res. Bull*. **1994**, *29*, 1297.
(81) Li, D.; Fleet, M. E.; Bancroft, G. M.; Kasrai, M.; Pan, Y. *J. Non-Cryst. Solids* **1995**, *188*, 181.
(82) Murashov, V. V.; Leszczynski, J. *J. Phys. Chem. A* **1999**, *103*, 1228.
(83) Bolt, G. H. *J. Phys. Chem.* **1957**, *61*, 1166.
(84) Tossell, J. A.; Sahai, N. *Geochim. Cosmochim. Acta.*, accepted.
(85) Hayes, K. F. Equilibrium, spectroscopic and kinetic studies of ion adsorption at the oxide/aqueous interface. Ph.D. Thesis, Stanford University, Stanford, 1987.

(86) Dzombak, D. A.; Morel, F. M. M. *Surface Complexation Modeling. Hydrous Ferric Oxide*; John-Wiley-Interscience: New York, 1990; pp 106, 173, 187, 300.
(87) Hayes, K. F.; Katz, L. E. In *Physics and Chemistry of Mineral Surfaces*; Brady, P. V., Ed.; CRC Press: Boca Raton, FL, 1996; pp 170, 178, 212.
(88) Sahai, N.; Carroll, S. A.; O'Day, P. A.; Roberts, S. *J. Colloid. Interface Sci.* **2000**, *222*, 198.
(89) Nancollas, G. H.; Zhang, J. In *Hydroxyapatite and Related Materials*; Brown, P. W., Constanz, B., Eds.; CRC Press: Boca Raton, FL, 1994; p 73.
(90) Tossell, J. A.; Saghi-Szabo, G. *Geochim. Cosmochim. Acta* **1997**, *61*, 1171.
(91) Onuma, K.; Ito, A. *Chem. Mater*. **1998**, *10*, 3346−3351.
(92) Larson, M. A.; Garside, J. J. *J. Cryst. Growth* **1986**, *76*, 88.
(93) Sohnel, O.; Garside, J. J. *J. Cryst. Growth* **1988**, *89*, 202.
(94) Christoffersen, M. R.; Christoffersen, J. J. *J. Cryst. Growth* **1992**, *121*, 617.
(95) Nielsen, E. A. *J. Cryst. Growth* **1984**, *67*, 289.
(96) Nanchollas, G. H.; LoRe, M.; Perez, L.; Richardson, C.; Zawacki, S. J. *Anatomical Rec.* **1989**, *224*, 234, in Onuma and Ito, cited above.
(97) Christoffersen, J.; Christoffersen, M. R.; Johansen, T. J. *J. Cryst. Growth* **1996**, *163*, 304.
(98) Yamashita, K.; Oikawa N.; Umegaki, T. *Chem. Mater*. **1996**, *8*, 2697.
(99) Aksay, I. A. *Materials Research Society Abstracts*, Fall Meeting, Boston, 1999; p 549.
(100) Kanzaki, N.; Onuma, K.; Ito, A.; Teraoka, K.; Tateishi T.; Tsutsumi, S. *J. Phys. Chem. B* **1998**, *102*, 6471−6476.
(101) Harrison, C. C. *Phytochemistry* **1996**, *41*, 37.
(102) Perry, C. C.; Lu, Y. *J. Chem. Soc., Faraday Trans*. **1992**, *88*, 2915.